

DTIC FILE COPY

4

AD-A217 991

**FERRITE RESEARCH AIMED AT IMPROVING INDUCTION
LINAC DRIVEN FEL PERFORMANCE**

Prepared by
Dr. Daniel Birx

SCIENCE RESEARCH LABORATORY, INC.
15 Ward Street
Somerville, MA 02143

8 February 1990

PHASE I FINAL REPORT

Period for August 15, 1989 to February 14, 1990

Contract Number N00014-89-C-0197

DTIC
S ELECTE D
FEB 14 1990
D

APPROVED FOR PUBLIC RELEASE; DISTRIBUTION UNLIMITED

Prepared for
OFFICE OF NAVAL RESEARCH
800 North Quincy Street
Arlington, VA 22217-5000

"The views and conclusions contained in this document are those of the authors and should not be interpreted as representing the official policies, either expressed or implied, of the Strategic Defense Initiative Organization or the U.S. Government."

90 02 13 074

REPORT DOCUMENTATION PAGE

Form Approved
OMB No. 0704-0188

1a. REPORT SECURITY CLASSIFICATION Unclassified			1b. RESTRICTIVE MARKINGS		
2a. SECURITY CLASSIFICATION AUTHORITY			3. DISTRIBUTION/AVAILABILITY OF REPORT Approved for Public Release; Distribution Unlimited		
2b. DECLASSIFICATION/DOWNGRADING SCHEDULE					
4. PERFORMING ORGANIZATION REPORT NUMBER(S) SRL-5-F-1990			5. MONITORING ORGANIZATION REPORT NUMBER(S)		
6a. NAME OF PERFORMING ORGANIZATION Science Research Lab		6b. OFFICE SYMBOL (If applicable)	7a. NAME OF MONITORING ORGANIZATION Office of Naval Research		
6c. ADDRESS (City, State, and ZIP Code) 15 Ward St. Somerville, MA 02143			7b. ADDRESS (City, State, and ZIP Code) Dept. of the Navy 800 N. Quincy St. Arlington, VA 22217		
8a. NAME OF FUNDING/SPONSORING ORGANIZATION SDIO		8b. OFFICE SYMBOL (If applicable)	9. PROCUREMENT INSTRUMENT IDENTIFICATION NUMBER N00014-89-C-0197		
8c. ADDRESS (City, State, and ZIP Code) Pentagon Washington, DC			10. SOURCE OF FUNDING NUMBERS		
			PROGRAM ELEMENT NO.	PROJECT NO. 1262	TASK NO.
			WORK UNIT ACCESSION NO.		
11. TITLE (Include Security Classification) Ferrite Research Aimed at Improving Induction Linac Driven FEL Performance					
12. PERSONAL AUTHOR(S) Dr. Daniel Bix and Dr. Joseph Mangano					
13a. TYPE OF REPORT Final		13b. TIME COVERED FROM 8/15/89 TO 2/14/90		14. DATE OF REPORT (Year, Month, Day) 1990/2/8	
15. PAGE COUNT 71					
16. SUPPLEMENTARY NOTATION					
17. COSATI CODES			18. SUBJECT TERMS (Continue on reverse if necessary and identify by block number)		
FIELD	GROUP	SUB-GROUP	Induction Accelerators, Ferrite Materials, Free Electron Lasers		
19. ABSTRACT (Continue on reverse if necessary and identify by block number) The objective of this effort is to develop compact, lightweight, low cost induction linear accelerator technology for driving space-based and ground based free electron lasers. In the Phase I effort, a new understanding of the role of the ferrite isolation lines used in induction accelerators was established and a relevant data base on the nonlinear properties of ferrite materials under short pulse excitation was obtained experimentally. This effort has resulted in the invention of a new architecture for linear induction accelerators. This new architecture leads directly to a factor of 6 increase in accelerator gradient, more than a factor of 10^2 decrease in accelerator weight and more than a factor of 3 decrease in accelerator cost while simultaneously improving electron beam brightness. These compact, lightweight low cost accelerators can then be used to develop affordable free electron laser devices which have a broad spectrum of military applications,					
20. DISTRIBUTION/AVAILABILITY OF ABSTRACT <input type="checkbox"/> UNCLASSIFIED/UNLIMITED <input checked="" type="checkbox"/> SAME AS RPT. <input type="checkbox"/> DTIC USERS			21. ABSTRACT SECURITY CLASSIFICATION		
22a. NAME OF RESPONSIBLE INDIVIDUAL			22b. TELEPHONE (Include Area Code)		22c. OFFICE SYMBOL

which include strategic and tactical missile defense and ground based laser ASAT as well as commercial applications in medicine and laser metal working.

TABLE OF CONTENTS

<u>Section</u>		<u>Page</u>
1.0	INTRODUCTION	1-1
1.1	Length of Conventional Linear Induction Accelerators	1-1
1.2	Accelerator Weight, Electron Beam Brightness and Cost	1-1
1.3	A New Linear Induction Accelerator Architecture	1-3
2.0	ROLE OF FERRITE MATERIALS IN INDUCTION LINAC OPERATION	2-1
2.1	Ferrite and Nonlinear Magnetic Pulse Compressors	2-3
2.1.1	Nonlinear Magnetic Material Selection	2-6
2.2	Ferrite in Accelerator Cells	2-9
2.2.1	Operating Voltage and Gradient	2-14
2.3	Characterization of Loss in Ferrite Materials	2-20
2.3.1	Ferromagnetic Resonance	2-22
2.4	Ferrite Sample Measurements	2-30
2.5	Cooling of Ferrite Cores	2-33
2.6	Using Ferrite to Control Dipole Wake Fields	2-44
3.0	NEW INDUCTION ACCELERATOR ARCHITECTURES	3-1
3.1	Summary of Phase I Effort	3-12



Accession For	
NTIS CRA&I	<input checked="" type="checkbox"/>
DTIC TAB	<input type="checkbox"/>
Unannounced	<input type="checkbox"/>
Justification	
By	
Distribution /	
Availability Codes	
Dist	Avail and/or Special
A-1	

LIST OF ILLUSTRATIONS

<u>Figure</u>		<u>Page</u>
1	Real and imaginary parts of the permeability as a function of frequency	2-2
2	Typical nonlinear magnetic pulse compressor operation	2-5
3	Estimated core loss versus saturation time in metglass tapes	2-7
4	Metglass characteristics	2-10
5	Simplified cross section of a conventional induction accelerator cell	2-13
6	Coupling coefficient	2-17
7	Accelerator core volume per megavolt	2-18
8	Loss tangent defined for a parallel LR circuit	2-21
9	Processional motion of a spinning symmetrical top in a gravitational field. The precession of the rigid body at frequency ω_0 is shown schematically in (a), and the angular momentum and torque vectors are shown in (b).	2-24
10	Real part of the initial permeability as a function of frequency for various ferrite materials	2-26
11	Experimentally-measured permittivity and resistivity for two zinc-nickel compositions	2-29
12	Temperature dependence of the permittivity and resistivity of two zinc-nickel compositions	2-31
13	B-H loop measurements	2-32
14	Hysteresis curves for various ferrite materials measured at $\tau_{sat} = 50$ nsec	2-34
15	Hysteresis curves for various ferrite materials measured at $\tau_{sat} = 100$ nsec	2-35
16	Hysteresis curves for various ferrite materials measured at $\tau_{sat} = 250$ nsec	2-36
17	Hysteresis curves for various ferrite materials measured at $\tau_{sat} = 500$ nsec	2-37
18	Energy dissipated per unit volume as the flux swings between $-B_r$ and B_s versus Saturation Time	2-38
19	Energy dissipated per unit volume divided by ΔB^2 in Tesla versus Saturation Time	2-39
20	Energy dissipated per unit volume divided by ΔT versus Saturation Time	2-40

LIST OF ILLUSTRATIONS CONTINUED

<u>Figure</u>		<u>Page</u>
21	Cooling of ferrites used in accelerator cells at a repetition rate of 10^4 pps	2-43
22	Test fixture and design considerations	2-47
23	RF attenuation in solid ferrite	2-48
24	$\text{Re}(\mu_r)$ calculated from $(\mu_r \epsilon_r)^{1/2}$ assuming $\epsilon_r(\omega) = \epsilon_r(\omega) = 1$ MHz	2-49
25	$ \mu_r ^+$ calculated from $(\mu_r/\epsilon_r)^{1/2}$ and $(\mu_r \epsilon_r)^{1/2}$ assuming $\epsilon_r(\omega) = \epsilon_r _{1\text{MHz}}$	2-50
26	Impedance of ferrites normalized to free space impedance (377Ω)	2-51
27	Inverse wave speed in ferrite normalized to c^{-1}	2-52
28	Simplified induction linear accelerator schematic	3-2
29	Conventional linear induction accelerator design	3-3
30	Concept I - Modified linear induction accelerator	3-5
31	Concept II: Ferriteless induction accelerator for short pulse operation	3-6
32	Concept III - Modified induction accelerator	3-11

1.0 INTRODUCTION

Compact, lightweight, low cost linear induction accelerators delivering high brightness electron beams are essential to the development of efficient ground- and space-based free electron lasers for strategic defense. Linear induction accelerators lead to high gain free electron lasers which are directly scalable to the ultra-high average power required by SDI applications. Science Research Laboratory has invented a new linear induction accelerator architecture which leads to a factor of 6 reduction in accelerator length, more than a factor of 10^2 reduction in accelerator weight and more than a factor of 3 reduction in accelerator cost while simultaneously allowing an increase in electron beam brightness by suppressing the growth of the beam break-up instability.

1.1 Length of Conventional Linear Induction Accelerators

Currently, linear induction accelerators are characterized by a low accelerating gradient (<0.5 MeV/meter) which leads to accelerator lengths of greater than 300 meters to generate the ~ 150 MeV electron beam required to drive a $1 \mu\text{m}$ wavelength free electron laser. In conventional induction linacs, the accelerating gradient is directly proportional to the length of the ferrite cores placed between the accelerating gaps and around the beam tube and its associated magnetic focussing coils. The length of these ferrite cores is in turn directly proportional to the pulse length. Therefore, the accelerator gradient in a conventional long pulse duration (50 nsec) accelerator is constrained to a low value determined by the voltage per gap V_{gap} (~ 150 kV), the pulse length t_p and the electromagnetic properties (ϵ_r, μ_r) of the ferrite material.

$$\text{Accelerating Gradient} = \frac{\sqrt{\epsilon_r \mu_r}}{ct_p} V_{gap} < 0.5 \text{ MeV/meter}$$

1.2 Accelerator Weight, Electron Beam Brightness and Cost

The weight of conventional linear induction accelerators is dominated by the total ferrite core weight which is given as

$$W = \rho_F \times \text{Ferrite Volume} = \rho_F l \pi (R_o^2 - R_i^2)$$

where

$$\rho_F = \text{mass density of the ferrite material}$$

l = length of the ferrite core

R_i = inner radius of the ferrite core

R_o = outer radius of the ferrite core

As discussed above, the length of the ferrite cores is determined by the pulse length and the electromagnetic properties of the ferrite materials

$$l = \frac{ct_p}{\sqrt{\epsilon_r \mu_r}}.$$

In conventional induction linac designs, the inner radius of the ferrite cores is determined by a trade-off between beam brightness and the volume and cost of the ferrite material used. High electron beam brightness requires suppression of the beam break-up instability growth rate which leads to a large beam tube radius and inner ferrite core radius. However, the larger the inner radius of the ferrite core, the larger the volume of ferrite required. The radial thickness of the ferrite and therefore its outer radius is determined by the drive voltage and the maximum flux swing available from the nonlinear ferrite material. The maximum flux swing available from a ferrite material and associated hysteresis losses are a function of the pulse length. The analysis which determines the outer core radius is somewhat complex and is discussed in more detail later in this proposal. However, at the maximum gap voltages allowed by field emission in the gap (~ 150 kV), the volume of core material scales approximately as R_i^2 .

Extremely high brightness electron beams are required for free electron laser applications. Beam brightness is determined by the electron gun design and its cathode emission properties and by beam transport through the accelerator. High brightness cathodes for free electron lasers are being developed in other research efforts and work is focussed on improving thermionic and photoemitting cathode technologies. Beam brightness degradation in beam transport through the accelerator is driven by the beam break-up instability. The exponential growth rate of this instability is proportional to R_i^{-2} . Consequently, high brightness electron beams can only be obtained when the diameter of the beam pipe is large (~ 30 cm for typical $1 \mu\text{m}$ wavelength FEL applications). This large beam pipe diameter then drives the volume of the ferrite material as discussed above. For example, it is estimated that approximately 2×10^5 kg of ferrite material

would be used in the construction of a conventional 50 nsec linear induction accelerator which delivers an electron beam of sufficient brightness and energy to drive a $1\text{ }\mu\text{m}$ FEL. It is critical to recognize that in conventional induction linac designs, the length, weight, and cost of the accelerator are directly related to the placement of the ferrite cores around the electron beam tube.

1.3 A New Linear Induction Accelerator Architecture

Science Research Laboratory has recently developed a new linear induction accelerator architecture which significantly reduces accelerator length, weight and cost. This new accelerator architecture places the ferrite cores which isolate the voltage between accelerating gaps around the coaxial drive lines instead of around the beam tube. This new accelerator design also operates with a significantly shorter pulse length – 5 to 10 nsec – than conventional linear induction accelerators (50 nsec pulse duration). These two features are directly responsible for the performance improvements discussed above.

The reasons for the significant increase in accelerator gradient are immediately apparent from the preceding discussion. By placing the ferrite cores around the coaxial drive lines, the distance between accelerating gaps can be decreased by a factor of approximately 6 with a corresponding decrease in accelerator length. The volume of ferrite can also be decreased for two reasons. First, the diameter of the coaxial cable which serve as the drive for each accelerator cell has a radius which is approximately 3 cm versus the 30 cm diameter of the beam tube. This consideration alone reduces the volume of the ferrite cores by a factor of approximately 10^2 with a corresponding decrease in accelerator weight. In addition, since the pulse length has been decreased by a factor of 5 or 10, the length of the ferrite cores can be decreased by a similar factor. These considerations taken together can reduce the total weight of the accelerator by a factor of as much as 10^3 . It is critical to note, however, that to maintain the same average electron beam power at fixed accelerator energy, current and accelerating gap voltage, the repetition rate must be increased by a corresponding factor of 5 or 10 from approximately 5×10^3 pps to 5×10^4 pps. This increase in repetition rate can be accomplished with the all-solid-state nonlinear magnetic

pulse compressor technology already being developed by SRL in a separate program. Reduction in ferrite costs, which dominate the material costs of linear induction accelerators of conventional design, lead directly to greater than a factor of 3 reduction in overall accelerator costs. This new accelerator architecture has an additional feature – the beam break-up instability can be suppressed by increasing the diameter of the beam tube without increasing the weight and cost of the accelerator.

Placement of the ferrite cores around the coaxial drive lines of the accelerator rather than around the beam pipe implies that high transient voltages are now present on the outside of the accelerator cells. This dipole field is oriented along the axis of the accelerator and has a peak voltage given by

$$V_{peak} = \frac{\text{Accelerator Gradient} \times \text{Pulse Length} \times c}{2}$$

For an accelerator gradient of 3 MeV/meter and a 5 nsec pulse duration, the peak voltage is approximately 2.25 MeV. However for ground based applications, the accelerator must be placed in a tunnel to shield against ionizing radiation induced by the electron beam. With a typical tunnel radius of 10 feet, this dipole electric field can easily be sustained in ambient air since the dipole fields decay as $1/r^2$ as they travel down the length of the accelerator at near the speed of light. For space-based applications, these fields can be contained in an inexpensive lightweight conducting tube which would surround the accelerator or they can simply be allowed to radiate into space.

2.0 ROLE OF FERRITE MATERIALS IN INDUCTION LINAC OPERATION

In this section, a detailed description of the Phase I results will be provided. Section contents include a technical description of the role of ferrites in the construction of high power linear induction accelerators, a summary of the Phase I experimental results, and a detailed discussion of new compact, lightweight linear induction accelerator architectures developed in Phase I.

Ferrite materials and their properties play a dominant role in the design and fabrication of high power linear induction accelerators. Ferrites with various compositions and performance parameters are now being tested and we will present the results below. A wide variety of candidate materials exist, but simple rules hold common to all candidate ferrites and allow one to predict which mixtures will be optimum. With the exception of the hexagonal ferrites used as permanent magnets, all ferrites share a common crystal structure, a cubic spinel. The chemical composition is $X \cdot Fe_2O_4$ where X can be any divalent metal or combination thereof. The use of different metals will result in different coupling coefficients between the spin moments and the lattice. This coupling is related to the initial permeability - the lower the permeability, the stronger the value of this coupling.

In the remanent state the spins align with neighbors in a domain. These domains form in such a way that the magnetic field energy is minimized. This corresponds to an alignment such that the external field is zero. When forced to change states of magnetization, the spins precess about the direction of the internal magnetic field. As damping occurs, the spins align with the applied magnetic field. For a nonconducting ferrite, as the rate of change of magnetization increases, the losses remain nearly constant until the ferrimagnetic spin precession resonance is reached. The lower the coupling constant (i.e. the higher the initial permeability), the lower this resonant frequency will be. Operating a ferrite in the proximity of this resonance results in a dramatic increase in losses and thereby in greatly increased cooling requirements. The curves for the real and imaginary components of the complex permeability for a ferrite very similar to the PE-11 ($Zn_{0.6}Ni_{0.4}$) $\cdot Fe_2O_4$ ferrite used in the ATA accelerator at LLNL are given in Fig. 1. The resonant frequency for this material is ~ 8 MHz corresponding to a saturation time of \sim

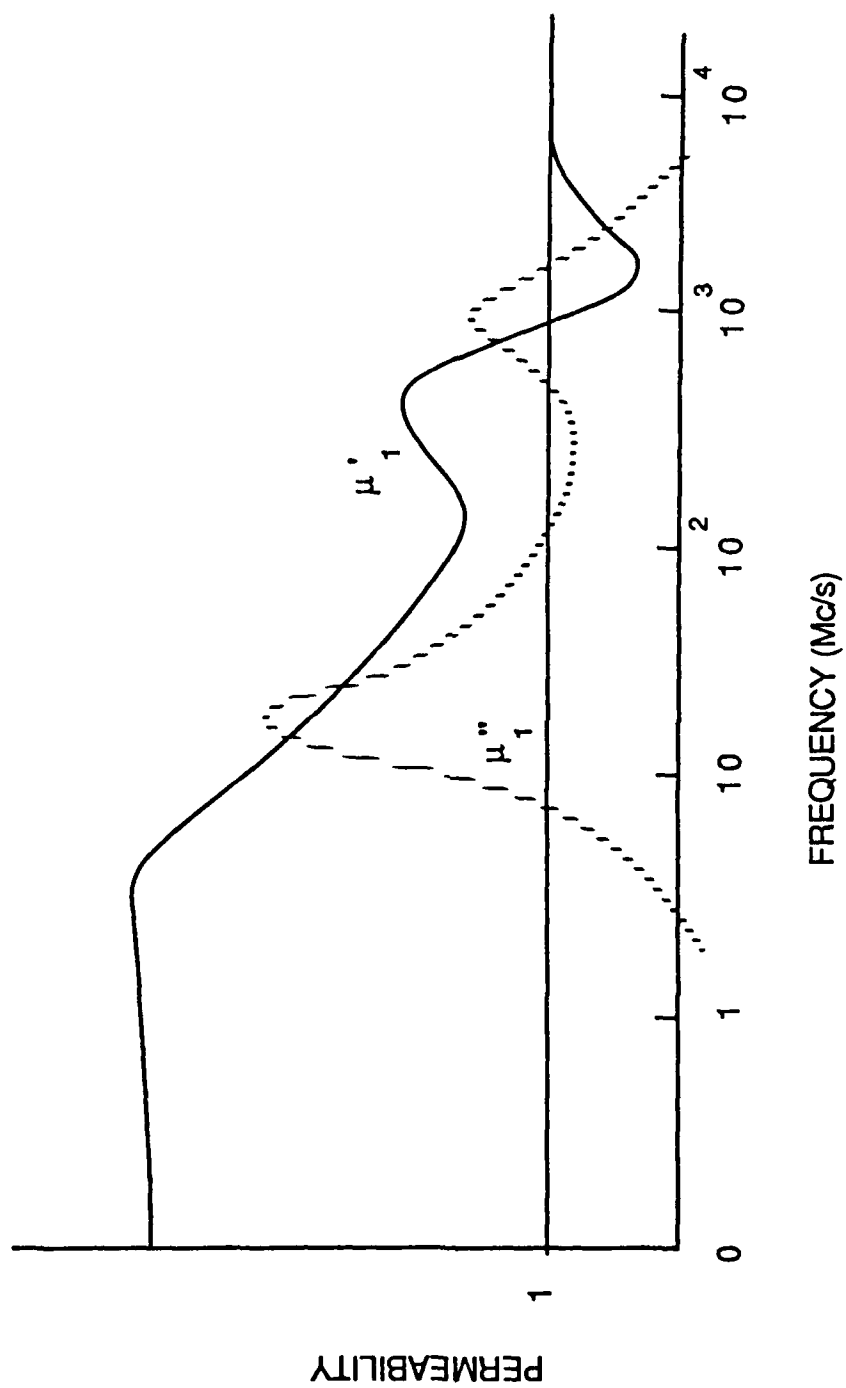


Figure 1: Real and imaginary parts of the permeability as a function of frequency

60 ns. This resonant frequency as mentioned above can be predicted by simply knowing the dc value of the initial permeability and the saturation magnetization.

Unfortunately optimization is not as simple as choosing a ferrite with a low value of initial permeability. The hysteresis losses increase approximately linearly with the inverse of the permeability in the absence of the resonance. The biasing field requirement is also increased further complicating the core reset circuits.

A ferrite should be chosen to have the highest possible permeability for a given operating frequency without incurring ferrimagnetic spin precession resonance. At this frequency, the losses increase dramatically as indicated by the large increase in the imaginary component of the permeability shown in Fig. 1. This resonant frequency is given by:

$$\nu_{res} = \frac{\gamma \cdot M_{sat}}{3 \cdot \pi \cdot (\mu_i - 1)}$$

where:

γ = gyromagnetic ratio ($\sim 0.22 \times 10^6$)

M_{sat} = Saturation magnetization ($2.5 \rightarrow 3.5 \times 10^5$ A/M)

μ_i = Initial permeability as $\nu \rightarrow 0$.

2.1 Ferrite and Nonlinear Magnetic Pulse Compressors

Ferrites play two key roles in induction linear accelerator design. They are employed in the final compression stages of the nonlinear magnetic pulse compressor and are also used as the core material in the accelerator cells. Before identifying an optimum ferrite composition, it is necessary to determine the desired operating characteristics. In this section we will examine the requirements for constructing efficient Nonlinear Magnetic Pulse Compressors.

Nonlinear magnetic pulser compressors are themselves resonant circuits. The basic principle underlying nonlinear magnetic driver operation involves using a saturable core which is an inductor in a resonant circuit. The circuit is designed to allow the core of the next stage to saturate before a significant fraction of the energy stored in the capacitors of the previous stage is transferred. This nonlinear saturation phenomenon shifts the resonant frequency of this

resonant circuit by the square root of the permeability shift as the core saturates. These stages are typically cascaded (Fig. 2) and energy is coupled faster and faster from one stage to the next. These circuits are efficient at transferring power in both directions since they act not only to upshift the frequency in the forward direction thereby providing temporal compression, but also downshift the frequency of a voltage pulse as it cascades back up the chain in the reverse direction. The energy which reflects from the mismatched load can propagate back up the chain to the SCR commutator.

Nonlinear Magnetic Pulse Compressors sometimes called "Magnetic Switches" take advantage of the large change in permeability of a ferro (ferri) magnetic material as it saturates. It is possible to achieve large factors ($>10^3$) of temporal pulse compression and thereby obtain the required power gain by employing saturable materials as inductor cores. Magnetic switches are beginning to appear in a large number of long life, high repetition rate pulsed power systems. They are presently being used to drive induction linear accelerators and are also employed as drivers of copper vapor lasers for the Atomic Vapor Laser Isotope Separation (AVLIS) program. Here large numbers of drivers are required to operate at 5000 pps continuously for time scales measured in years. SRL is assisting in developing advanced, all solid state drivers for both of these programs.

The design of efficient high gain pulse compression stages relies on the careful control of the magnetic fields surrounding the core volume. The losses in a compression stage are linearly proportional to the volume of core material used and it can be shown that the core volume requirement for this saturable inductor is given by:

$$\text{volume} = \text{gain}^2 \cdot \text{Pulse Energy} \cdot \left(\frac{\mu_0 \cdot \pi^2}{4 \cdot (\Delta B_s \cdot \text{pf})^2} \right) \quad (2.1)$$

where ΔB_s is the available flux swing of the material (with appropriate biasing given by $+B_s - (-B_s) = 2B_s$), gain is defined as the temporal compression factor (τ charge/ τ discharge), and pf is the packing factor. The packing factor is defined as

$$\frac{\int_{V_I} H^2 dv}{\int_{\text{all space}} H^2 dv} \quad (2.2)$$

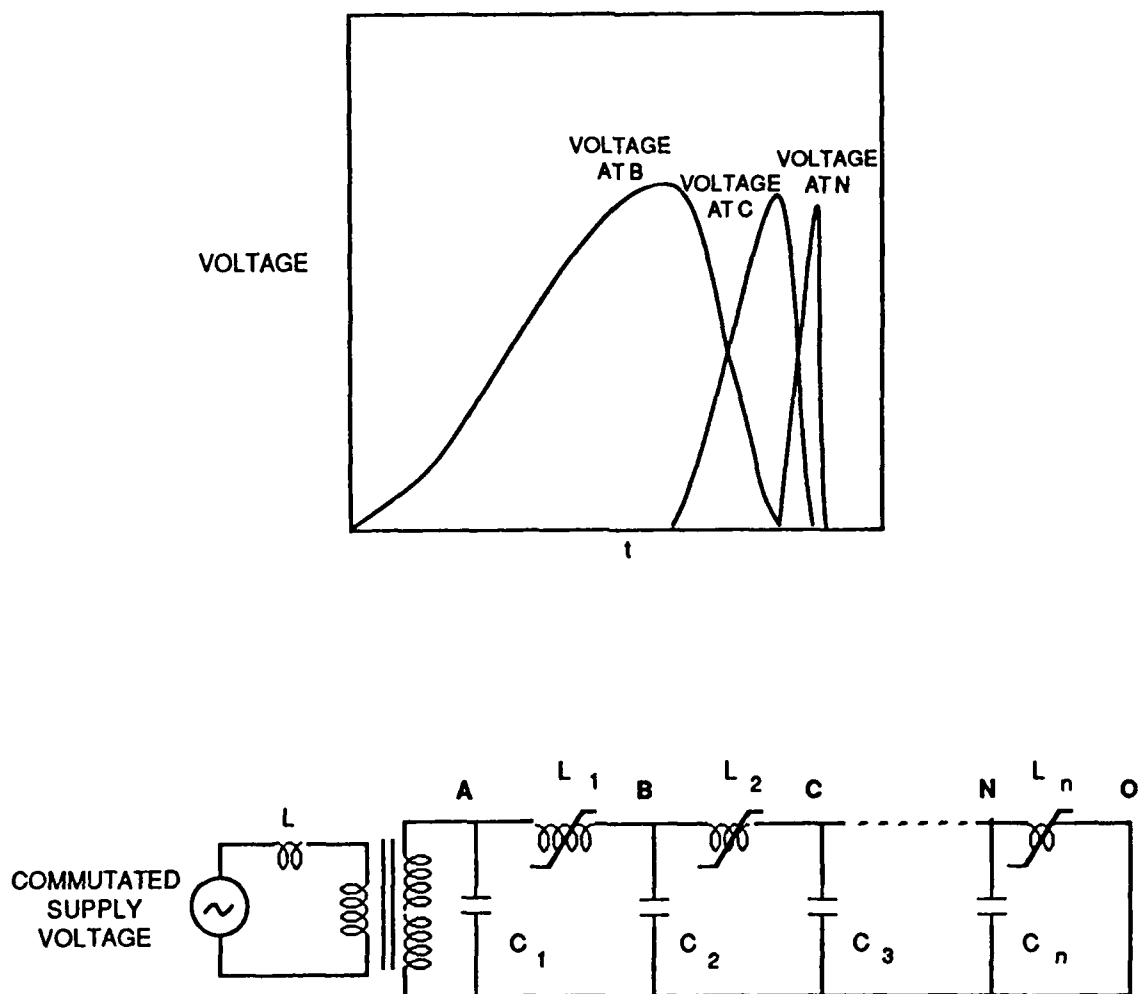


Figure 2: Typical nonlinear magnetic pulse compressor operation

where V_f is the actual volume occupied by the ferri- (ferro) magnetic core material excluding all interlaminar insulation and voids. Optimization of this packing factor is crucial in magnetic switch design and is accomplished by enclosing the core in a tightly fitting conducting housing. The multiple turns are formed as coaxial transmission lines which pass through this housing. Circulating currents set up in this housing exclude the magnetic flux and contain it in the desired volumes.

The core volume requirement scales with the inverse square of the ΔB_s and losses will vary linearly with the core volume. Therefore, loss per unit volume must be normalized by $(1/\Delta B_s)^2$ before a comparison between different materials can be made. In other words using a material with twice the loss per unit volume but twice the ΔB_s will decrease the loss by a factor of two since only one fourth the volume is required.

2.1.1 Nonlinear Magnetic Material Selection

It is important to understand when it is advantageous to use ferrite rather than metal tapes such as metglass in magnetic pulse compressors. In this section we will compare the attributes of ferrites with those of metal tapes. The first stage compression reactor step-up transformer and (sometimes) the second stage compression reactor are designed around metglass cores. This is the last stage in the compression chain where metglass can be employed if operation at greater than 5 kHz cw repetition rate is to be possible. Metglass is composed of a mixture of silicon and iron which is mixed while liquified and then rapidly quenched so that it remains amorphous. The resistivity of this alloy is three times that of most ferro-magnetic materials. However, at saturation times much less than 10^{-6} seconds, the losses begin to scale inversely with the saturation time as eddy currents become the dominant loss mechanism (see Fig. 3).

Further increases in performance can be achieved through basic material improvements. Drivers will predominately employ 2605 CO, SC and S3A Metglass as a saturable core material. These mixtures of silicon and steel possess the magnetic properties of steel (i.e. $\Delta B \sim 36$ kg, $H_c \sim 0.05$ Oe, $\mu_r \approx 10,000$) but afford much higher resistivities ($\rho \sim 130 \mu\Omega\text{-cm}$) because of its glass containing atomic structure. Unfortunately it has a rough surface texture resulting in

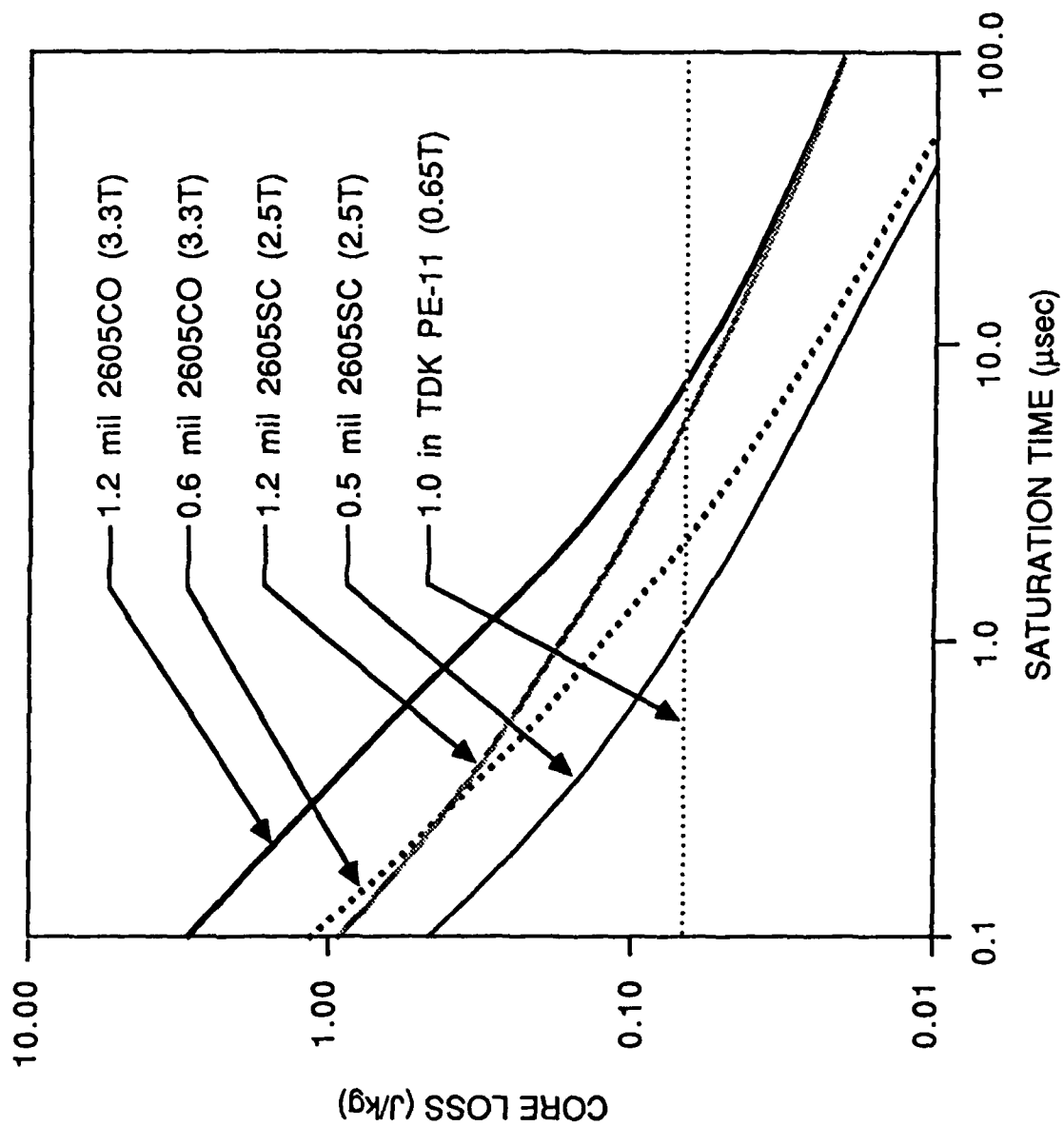


Figure 3: Estimated core loss versus saturation time in metglass tapes

inherent packing factors of only 0.75 and the addition of interlaminar insulation further reduces this to ~ 0.5 in a wound core. Interlaminar insulation can be avoided if the material can be vapor deposited with a very thin layer of MgO or SiO₂. The inherent 0.75 packing factor associated with roughness can be improved by hot rolling the metglass. These techniques are aimed at the objective of achieving an overall packing factor of 0.8.

Even with a packing factor of only 0.5 (compared to almost unity with ferrite), when the inherent $\Delta B_s \leq 3.3 \text{ Tesla}$ of metglass is compared to $\Delta B_s \leq 0.65 \text{ Tesla}$ of Zn₆₀Ni₄₀ ferrite (core volume depends inversely on ΔB_s^2), metglass is preferred when eddy current losses are not a problem. As the saturation times get shorter and eddy current losses increase, removing the waste heat from the interlaminar core structure becomes very difficult. Manganese zinc ferrites would seem a logical choice to span the gap between metglass and Zn₆₀Ni₄₀ ferrite, but geometric resonances encountered in the large cores required at high pulse energy eliminate it from consideration. Other iron alloys such as superpermalloy have been considered but suffer from the same heat removal problems as metglass. The higher conductivity of these alloys requires them to be thinner and this results in a greater expense and a lower net packing factor. It is hoped that advances in coating technology will improve the situation in the future.

The time dependent losses in ferro-magnetic are typically explained in terms of a saturation wave which encircles the tape and proceeds toward the center at a rate which is linearly dependent on the applied voltage. Ignoring the fact that domain wall locations are initially pinned to impurity sites, the H-field required to change the state of magnetization of a tape is given by

$$H_a = H_c + \left(\frac{d^2}{4\rho} \right) \left(\frac{\Delta B}{2B_s} \right) \left(\frac{dB}{dt} \right)$$

where B_s is the saturation induction, H_c is the DC anisotropy coercive field, d is the sample thickness and ρ is the resistivity. The energy density deposited in the tape during saturation is given by

$$E_L = H_c \Delta B + \left(\frac{d^2}{8\rho} \right) \left(\frac{\Delta B^2}{2B_s} \right) \left(\frac{dB}{dt} \right)$$

This theory assumes the metglass material is completely isotropic and possesses no preferred domain geometry. This is certainly not true and experimental measurements of time dependent

losses conducted by Dr. Carl Smith at Allied Chemical Research Laboratories indicate a much more complicated behavior. This data summarized in Fig. 3 is further documented by graphs prepared by Dr. Carl Smith which appear in Fig. 4.

The chart of loss versus saturation time in Fig. 3 points out that once normalized by $(1/\Delta B_s)^2$, metglass is the optimum material down to 100 nsec. saturation times and then ferrite must be used.

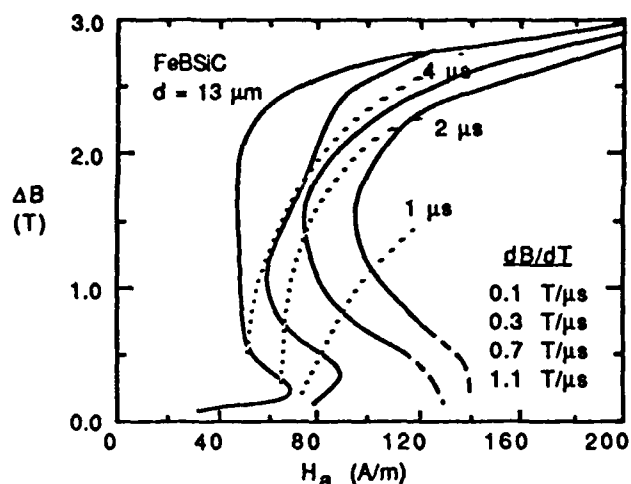
In the past, ferrite was sometimes used in cores when metglass was the best material choice. This was done because techniques for adequately cooling tape-wound cores had not been developed. This is no longer true and metglass is the optimum material for nonlinear magnetic compressor cores operating with ≥ 100 nsec saturation times.

2.2 Ferrite in Accelerator Cells

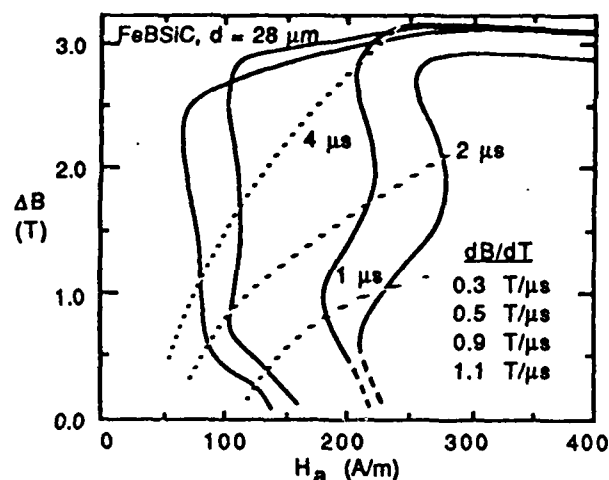
In the following section, we will discuss the considerations involved in the design of conventional induction accelerator cells. We will see the critical role played by the ferrite permeability. We will also show that the accelerator gradient and weight vary linearly with the pulse length.

Both RF and induction linear accelerators are composed of multiple transmission line transformers. While these transmission lines are all driven in parallel as the electron beam passes through them, their voltages add energy to the electron beam in series. Isolation between the transmission lines is achieved by connecting them with a beam pipe which is below cutoff at the operating frequency for all modes except the TEM_{00} . The electron beam forms the inner conductor for this mode. Early Soviet literature describes RF accelerators as air core induction linacs.

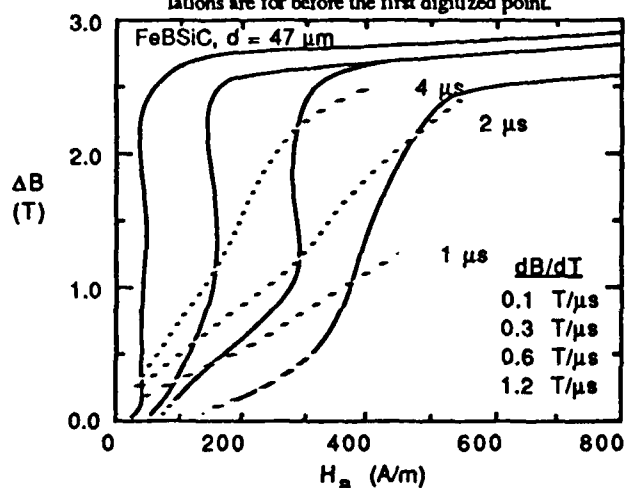
If the accelerator is to be efficient, the losses in the transmission line must be negligible in comparison to the energy coupled into the electron beam. In other words, the effective impedance of the transmission line Z_{eff} must be large compared to V_{LINE}/I_{BEAM} . For an RF accelerator, the characteristic line impedance Z_{LINE} may be low, less than 100 ohms, but it is resonant and therefore the effective impedance becomes $Z_{eff} = Z_{LINE} \cdot Q_L/2\pi$ (lowest order mode) where Q_L is the loaded Q of the resonant cavity.



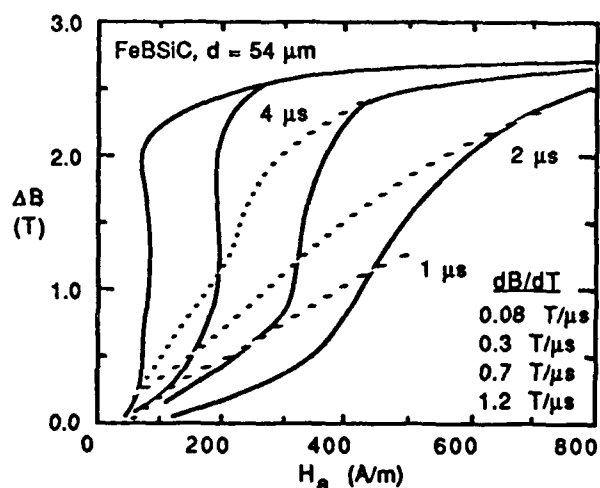
Dynamic magnetization and pulse permeability curves for 13 μm FeBSiC ribbon. Dashed extrapolations are for before the first digitized point.



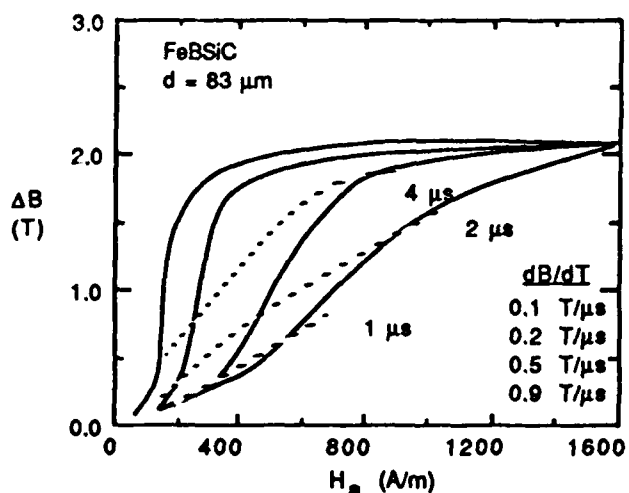
Dynamic magnetization and pulse permeability curves for 28 μm FeBSiC ribbon.



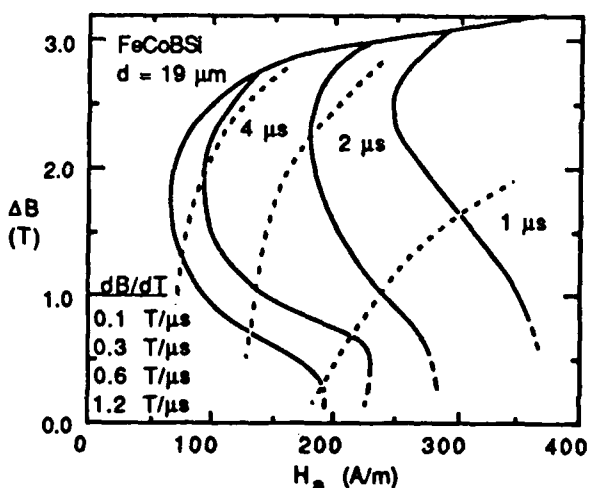
Dynamic magnetization and pulse permeability curves for 47 μm FeBSiC ribbon.



Dynamic magnetization and pulse permeability curves for 54 μm FeBSiC ribbon.



Dynamic magnetization and pulse permeability curves for 83 μm FeBSiC ribbon.



Dynamic magnetization and pulse permeability curves for 19 μm FeCoBSi ribbon.

Figure 4: Metglass characteristics

Resonant RF structures also have the advantage that they provide a voltage step up over the drive voltage by a factor.

$$V_{acc} = V_{driver} \cdot Q_L^*/2\pi$$

where:

$$Q_L^{*-1} = Q_s^{-1} + Q_e^{-1} + Q_{beamloading}^{-1}$$

The disadvantage of resonant structures is that a cavity (shorted $\lambda/2$ transmission line) is never simply resonant with a single mode and the wake functions of the electron beam have Fourier components which feed energy into all available modes. Some of these modes are spatially antisymmetric and act to steer the electrons into the beam pipe wall. This sets an upper limit to the total charge which can be accelerated during an RF cavity decay time ($\tau = Q_L/\omega$).

An induction cell is non-resonant and if designed properly stores neither the drive fields nor the wake fields. This dramatically increases the practical operating current but also places constraints on the minimum efficient operating current. If the induction accelerator cell used vacuum as a transmission line medium, the maximum impedance in practice would be less than a few hundred ohms. In operating induction linacs which provide short pulses (~ 50 ns), this line is filled with ferrimagnetic material (ferrite); for long pulses ($50 \text{ nsec} \leq \tau_p \leq 1 \mu\text{sec}$) ferromagnetic materials (e.g. Si-Fe, Metglass, Superpermalloy) are employed. Most high frequency ferrites have dielectric constants of order $\epsilon_r = 10$ and permeabilities of order $\mu_r = 1000$. With ferrite as a medium, the characteristic transmission line impedance is increased over the vacuum value by a factor of $(\mu_r/\epsilon_r)^{1/2} = 10$, yielding effective shunt impedances as high as several thousand ohms. Also the use of ferrite shortens the length of the transmission line required to provide isolation at the desired drive pulse length. Since the group velocity, $v_g = c/(\mu_r\epsilon_r)^{1/2} \simeq c/100$, the transmission line is shorter than the vacuum equivalent by a factor of order 100. Some low frequency RF accelerators employ ferrite solely for this purpose even though the line is resonant.

In summary the use of ferrite in the accelerator cell increases the practical micropulse length by a factor of 100 and the use of a non-resonant structure (induction linac) increases the maximum

electron beam current by not storing wake fields. The penalty accompanying these advantages is centered on the fact that induction accelerators are incapable of efficiently accelerating very low current beams.

Design of an induction accelerator cell is relatively straightforward if these basic operating principles are kept in mind. The following rules must be observed. The variables discussed refer to those pictured in Fig. 5.

I. The length (h) of the ferrite loaded transmission line is determined by the pulse length and the electrical characteristics of the ferrite.

$$2 \cdot h \geq \tau_p (\text{pulse length}) \cdot \text{velocity} \\ = \tau_p \cdot \frac{c}{\sqrt{\epsilon_r \mu_r}} \approx \frac{\tau_p \cdot c}{100}$$

In practice, the best performance is achieved by setting $h = \tau_p \cdot c/100$ or in other words setting the line length equal to a single transit time rather than a round trip time. This constraint arises because the ferrite properties are field dependent and the minimum ferrite volume is achieved by designing around a single transit time. Making h longer than a transit time is wasteful as the additional ferrite will never be seen by the pulse. Summarizing, for optimum performance:

$$h \approx \frac{\tau_p \cdot c}{(\epsilon_r \mu_r)^{1/2}} \approx \frac{\tau_p \cdot c}{100}$$

II. The value for $(R_o - R_i) = \Delta R$ is set by the drive voltage and the maximum flux swing of the ferrite. As the wave generated by the drive pulse is transmitted down the line, the creation of a saturation wave must be avoided or the impedance of the line will appear time dependent.

Since

$$\int E \cdot dl = - \frac{d}{dt} \int B \cdot da$$

if one assumes μ is constant and $B = \mu H$,

then

$$B \leq B_{sat}$$

Two extreme cases may be considered:

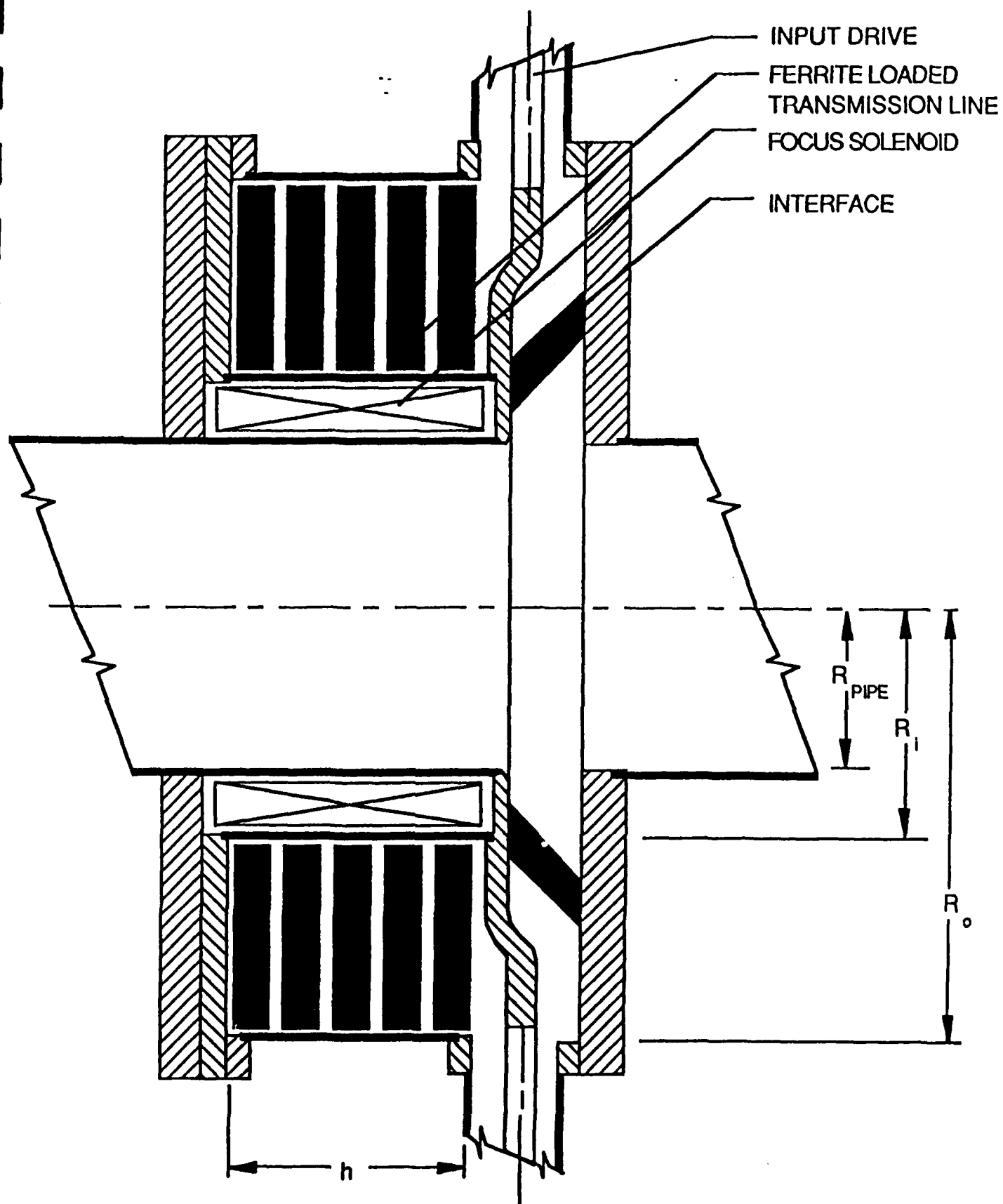


Figure 5: Simplified cross section of a conventional induction accelerator cell

A) If $B(r) = \text{const}$, then

$$\text{Voltage} \leq \Delta B_s \cdot \Delta R \cdot v_g$$

B) If $B(r) \propto 1/r$ and if no portion of the line is allowed to saturate

$$B(R_i) \leq B_{sat}$$

and

$$\text{Voltage} \leq \Delta B_s \cdot v_g \cdot R_i \cdot \ln(R_o/R_i)$$

In practice μ is not a constant and is dependent on both dB/dt and H . This causes the real requirement to lie somewhere in between cases (A) and (B) so that $B(r) \propto r^{-\alpha}$, $0 \leq \alpha \leq 1$.

III. Beam Pipe Radius - R_{PIPE}

Three competing requirements determine the optimum value for R_{PIPE} :

(A) The growth of the beam break-up instability (BBI) is exponentially dependent on R_{PIPE}^{-2} .

(i.e. $A = A_o \exp(I_{BEAM} \cdot V_{acc} \cdot \text{Const.}/B_{kg} R_{PIPE}^2 \cdot E_{gap}))$

(B) The impedance of the ferrite loaded transmission line decreases approximately linearly with R_{PIPE}^{-1} .

(C) The weight of the accelerator increases as the square of R_{PIPE} .

In short the losses are increasing with R_{PIPE} linearly while the growth of BBI is decreasing exponentially as R_{PIPE}^2 . It is essential in these designs to fully understand the dependence of the growth rate of the BBI on pipe diameter. In past designs, the pipe diameter has been undersized and has resulted in designs which were not compatible with full current operation. This applies to both RF and induction linear accelerators.

2.2.1 Operating Voltage and Gradient

It has been shown above that the length of a conventional induction accelerator is set by the selection of core material and pulse length. In addition the beam pipe radius is determined primarily by BBI considerations. It was also shown that the value of $\ln R_o/R_i$ was determined by the core material and the individual gap drive voltage. Indeed once the drive voltage, current and pulse length are selected, then limiting values for the accelerator cell are uniquely determined.

The operating current, total accelerator voltage and pulse length are set by the application. This leaves the individual gap voltage the only unspecified parameter. We have shown above that the accelerator gradient is linearly proportional to the individual gap voltage. One must bear in mind that while the number of secondary turns N_{sec} is unity, the number of primary turns is fractional given by

$$N_{prim} = \frac{1}{\#Acc\ cells}$$

$$Z_{out} = \frac{V_{acc}}{I_{beam}}$$

while Z_{in} the input drive impedance to the individual cells is given by

$$Z_{in} = \frac{V_{gap}}{I_{percell}}$$

The shunt impedance to ground is determined by the accelerator cell geometry and choice of core material. It is given by

$$Z_{shunt} = \frac{1}{2\pi} \sqrt{\frac{\mu}{\epsilon}} \ln R_o / R_i$$

Under the assumption that no ferrite is allowed to exceed a flux swing of ΔB_s and $B(r) \propto 1/r$, we saw that the accelerator gap voltage was given by

$$V_{gap} = \Delta B_s \cdot v_g \cdot R_i \ln R_o / R_i$$

where $v_g = c/(\epsilon_r \mu_r)^{1/2}$ is the wave velocity in the ferrite, $R_i(R_o)$ the inner (outer) radius of the ferrite core. The accelerator shunt impedance is then simply determined by the characteristic impedance of this ferrite loaded transmission line

$$Z_{SHUNT} = Z_{LINE} = \frac{1}{2\pi} \sqrt{\frac{\mu}{\epsilon}} \ln \left(\frac{R_o}{R_i} \right) = \frac{1}{2\pi} \sqrt{\frac{\mu}{\epsilon}} \frac{V_{gap}}{v_g \cdot \Delta B_s \cdot R_i}$$

$$= \frac{1}{2\pi} \mu \cdot \frac{V_{gap}}{\Delta B_s \cdot R_i}$$

If the electron beam impedance is defined as

$$Z_{beam} = \frac{V_{gap}}{I_{BEAM}}$$

then the coupling coefficient (= energy coupled to the beam/the total energy incident on the accelerator cell) is given by

$$K = \frac{Z_{SHUNT}}{Z_{BEAM} + Z_{SHUNT}} = \frac{1}{\frac{2\pi\Delta B_s R_i}{\mu I_{BEAM}} + 1}$$

A plot of coupling coefficient versus ferrite core inner radius for several different beam currents appears in Fig. 6. Here we have assumed a ferrite with a $\mu_r = 400$ and $\epsilon_r = 12$.

It should be noted that the coupling coefficient is independent of accelerator gradient but increases with increasing current and decreasing ferrite core inner radius.

The cost and weight of the accelerator structure is to first order linearly dependent on the core column.

$$\text{Core Volume} = \# \text{cells} \cdot \text{cell core length} \cdot \pi(R_o^2 - R_i^2) \quad (2.3)$$

and

$$V_{gap} = \frac{V_{acc}}{\# \text{cells}} = \Delta B_s \cdot v_g \cdot R_i \ln(R_o/R_i) \quad (2.4)$$

if $B \propto 1/r$ and no ferrite is allowed to exceed a flux excursion of ΔB_s . We can then rewrite Eq. (2.3) as

$$\text{Core Volume} = \frac{V_{acc}}{V_{gap}} \cdot v_g \cdot \tau_{pulse} \cdot \pi R_i^2 \exp\left(\frac{V_{gap} \cdot 2}{\Delta B_s \cdot v_g \cdot R_i}\right)^{-1} \quad (2.5)$$

where τ_{pulse} is the pulse length. It should be noted that the minimum core volume (d core volume/d $V_{gap} = 0$) is always achieved when $V_{gap} = 0$. Also for $2 \cdot V_{gap} / \Delta B_s \cdot v_g \cdot R_i \ll 1$, core volume is approximately independent of V_{gap} while for

$$\frac{2V_{gap}}{\Delta B_s \cdot v_g \cdot R_i} \gg 1$$

core volume becomes exponentially dependent on V_{gap} .

This becomes obvious upon careful examination of Fig. 7. Here we have assumed $\mu_r = 400$, $\epsilon_r = 12$, and $\tau_{pulse} = 50$ nsec. Referring to Eq. (2.4), it also appears that core volume is linearly dependent on τ_{pulse} . The dependency on $v_g = c/(\mu_r \cdot \epsilon_r)^{1/2}$ is somewhat more subtle. For small values of V_{gap}/R_i the core volume varies as $1/\mu_r^{1/2}$ but as V_{gap}/R_i becomes large, core volume becomes exponentially dependent on $\mu_r^{1/2}$.

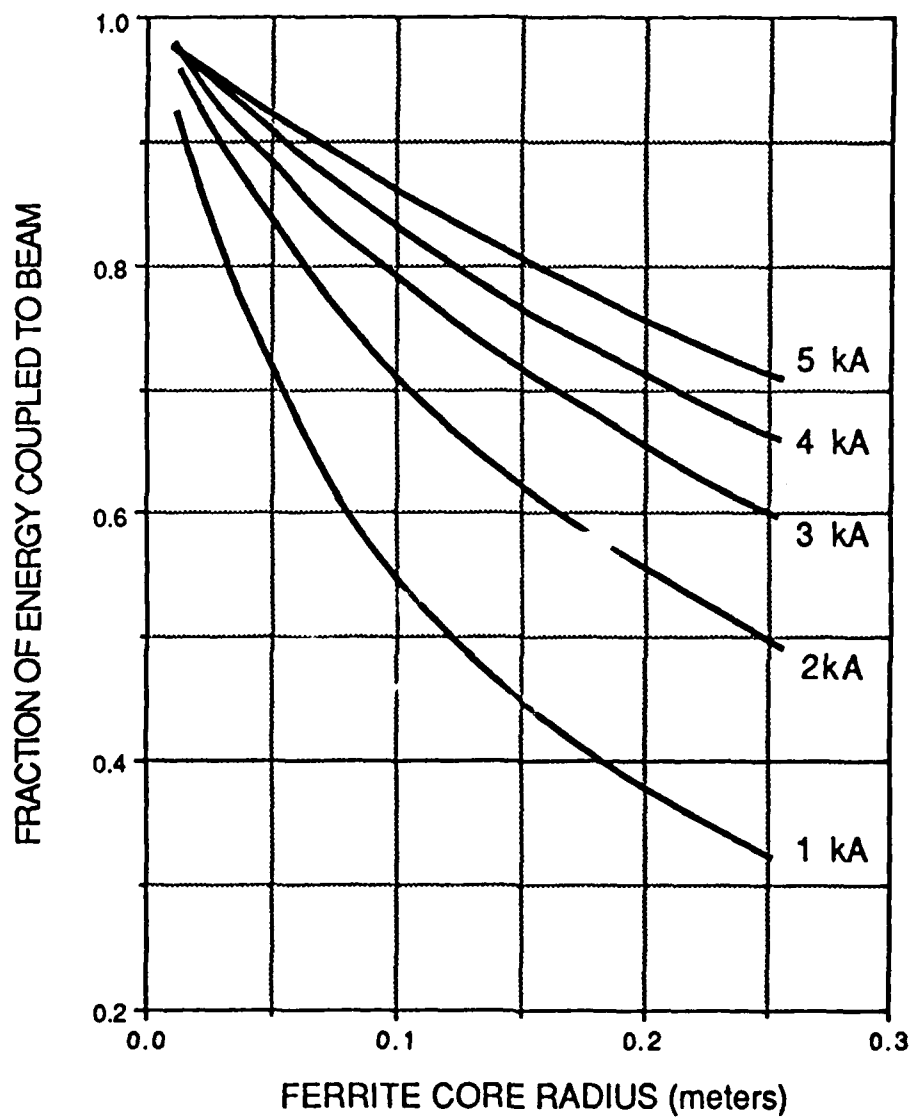
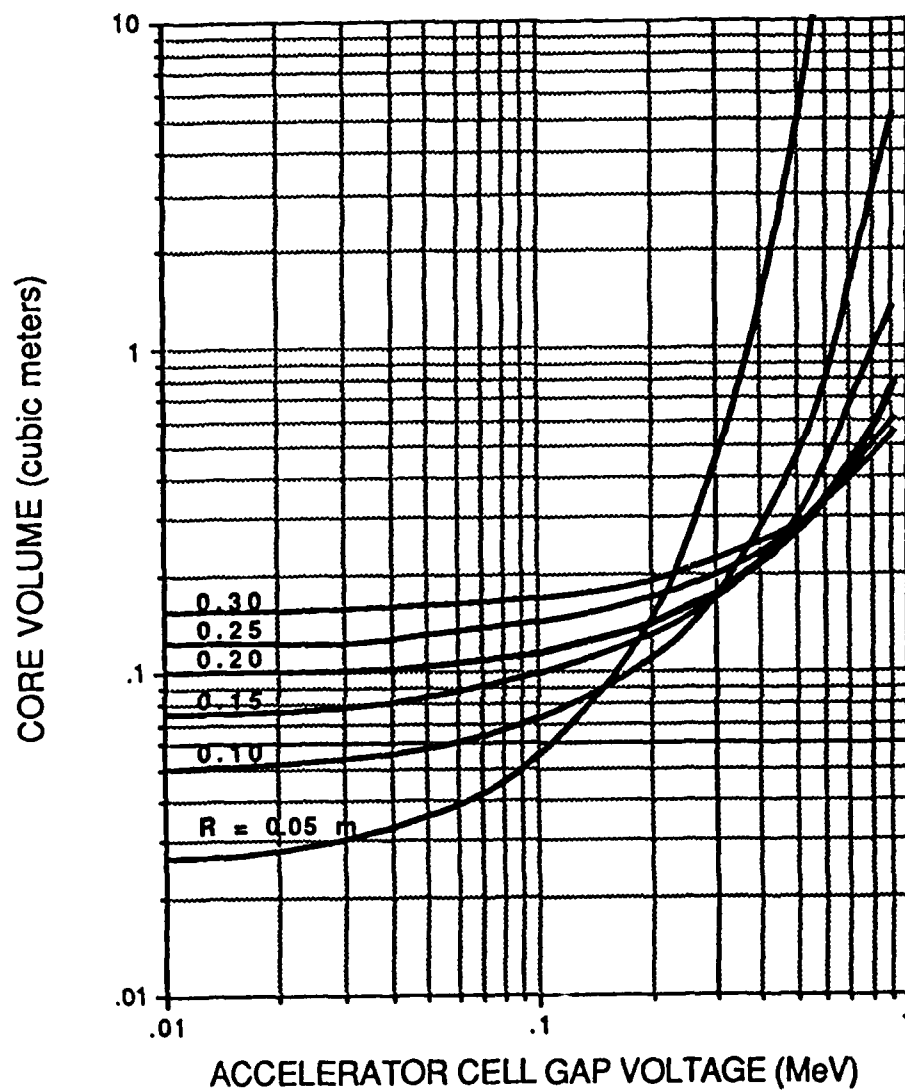


Figure 6: Coupling coefficient



$$\mu = 400, \Delta B_s = 0.65 \text{ Tesla}$$

Figure 7: Accelerator core volume per megavolt

It is also obvious from Fig. 7 that the inner ferrite core radius dramatically impacts the accelerator weight at a given gradient. Referring to Fig. 6 the efficiency degrades rapidly as the ferrite inner radius is increased. This inner radius is determined primarily by the beam pipe radius and the thickness of the focusing solenoid. Arbitrary reduction of these parameters independently of the current will result in the onset of the Beam Break-up Instability which will drive the accelerator beam current into the walls.

The amplitude of the BBI oscillation throughout the accelerator is given by:

$$A = A_0 \exp \left(\frac{\text{const.} N I Z_{\perp} \omega}{B_{kg}} \right)$$

where

$$K = 1.16 \cdot 10^{-13} \text{ kg} \cdot \text{sec}/(\text{kamp} \cdot \text{ohm})$$

$$N = \text{Number of accelerator gaps}$$

$$\omega = \text{Mode frequency}$$

$$I = \text{Accelerator current}$$

$$B_{kg} = \text{Focussing field}$$

Substituting

$$N Z_{\perp} = N (Z_{\perp} / Q) \cdot Q = \frac{\text{const.}_1 \cdot Q \cdot V_{acc}}{E_{gap} \cdot R_{pipe}}$$

where

$$V_{acc} = \text{Accelerator voltage}$$

$$E_{gap} = \text{Accelerator gap electric field stress}$$

$$R_{pipe} = \text{Beam pipe radius provides the following equation for the BBI amplitude.}$$

$$A = A_0 \exp \left(\text{const.} \cdot \frac{I \cdot V_{acc}}{B_{kg} R_{pipe}^2 \cdot E_{gap}} \right)$$

Therefore, the BBI amplitude depends exponentially on the inverse of the electric field in the accelerator gap and the beam pipe radius squared.

In order to minimize both the beam pipe radius and the solenoid thickness (B_z) while holding BBI gain constant at a given current and accelerating potential, the accelerator gap stress must

be increased to as high a value as practicable. Unfortunately at the high duty factors required for most of these applications, exceeding the threshold where field emission in the gap occurs is not allowed. Understanding this limit is essential to optimizing the design.

The core volume becomes exponentially dependent on the inverse of ΔB_s . This makes the design somewhat more complex as the individual gap voltages and beam pipe inner radius must be determined before the optimum material can be selected. At this point we will attempt to document the ferrite properties and the optimum choice will be left for the engineer responsible for a specific accelerator cell design.

2.3 Characterization of Loss in Ferrite Materials

Since ferrites are used primarily in pulse transformers where the shunt impedance is more important than the energy lost per pulse, the terminology used by the vendors to describe the losses is related to this application. It is worthwhile to devote a section in this report to the explanation of these units and the conversion of these units into units such as joules per meter³ per cycle.

Manufacturers typically quote loss data in terms of the phase angle, δ_m , between B and H. This angle is derived by first assuming resistive losses in the windings are zero and measuring the impedance of the core material when used as an inductor. The equivalent circuit illustrated in Fig. 8 is assumed. The shunt admittance is given as

$$Y = \frac{1}{i\omega L} + \frac{1}{R} = \frac{1}{Z}$$

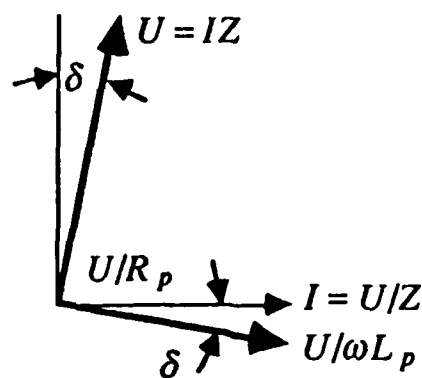
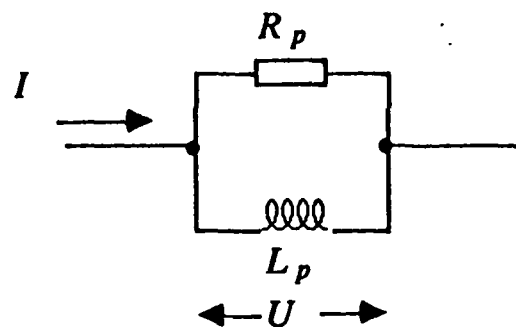
We will define shunt admittance in terms of the complex permeability as

$$\frac{1}{i\omega L} + \frac{1}{R} = \frac{1}{i\omega L_0} \left(\frac{1}{\mu_r} + \frac{i}{\mu_i} \right)$$

From this we define the loss tangent as the ratio of the real to imaginary part of the shunt admittance

$$\tan \delta_m = \frac{\omega L}{R} = \frac{\mu_i}{\mu_r}$$

In order to put this in terms of power loss density, we envision a toroid with N turns to which an alternating rms voltage V_{rms} is applied. The power loss density is then approximately



$$\tan \delta = \frac{\omega L_p}{R_p}$$

Figure 8: Loss tangent defined for a parallel LR circuit

given as

$$P \approx \frac{V_{rms}^2}{RA2\pi r}$$

where r is the mean core radius and A is the core cross sectional area. The applied voltage induces a changing flux density given by Faraday's law as

$$\frac{dB}{dt} = \frac{V}{NA}$$

If we assume B is of the form

$$B = B_0 e^{i\omega t}$$

then

$$V_{rms} = \frac{B_0 AN\omega}{\sqrt{2}}$$

The inductance of the winding can be approximated as

$$L_0 \approx \mu_0 \mu N^2 A / 2\pi r$$

Substituting we find the power loss density can be written as

$$P \approx \frac{\omega^2 B_0^2 L_0}{2R\mu\mu_0} \approx \frac{\omega B_0^2 \tan(\delta_m)}{2\mu\mu_0}$$

This expression works very well on approximating the losses in ferrite where the eddy current losses can be neglected and where the total flux excursion is small. It assumes that the B-H loop can be approximated as parabolic which is a fairly good approximation for minor loops where the total ΔB swing is less than 1/2 of $B_s - (-B_r)$. One of the reasons that this simple formula works so well is that the manufacturers assume this formula when quoting their loss measurements. It is quite simply a one parameter fit to a parabola.

2.3.1 Ferromagnetic Resonance

The concept of ferromagnetic resonance can best be understood by simple analogy to the precessional motion of a spinning top. The spinning electron may be treated as an electrically charged spinning mass. The magnetic forces acting on the spinning electron are similar to the gravitational forces acting on a spinning top. The magnetic forces acting on the electron in a

ferromagnetic material are derived from two primary sources. These two components consist of the internal magnetic fields generated by the many individual magnetic dipoles which make up the domains and secondly the external forces which when applied perturb the alignment of these dipoles. When the external fields are applied at an angle to the internal fields they exert a thrust or torque on the spinning electrons.

In the case of a spinning top (Fig. 9) application of a force perpendicular to the axis of spin will initiate precession. The precession frequency ω_0 depends on the angular momentum of the top and the gravitational force Mg acting on the center of mass of the top. The gravitational torque is

$$T = MgL \sin \theta$$

where θ is the angle of inclination and L is the distance from the pivot point to the center of mass. The angular momentum vector will maintain a constant angle θ with the vertical and the top will precess about the vertical axis with an angular velocity

$$\frac{d\phi}{dt} = \omega_0 = \frac{T}{p \sin \theta}$$

The spinning electron can be treated as a spinning top where the forces of gravity are replaced by the magnetic forces. In the case of a spinning electron the angular momentum and magnetic moment are parallel vectors with absolute values of p and μ_e . The gyromagnetic ratio is defined as

$$\gamma = -\mu_e/p = ge/2mc$$

where e is the electronic charge, m the electron mass, c the velocity of light and g is the Lande g -factor and is approximately equal to 2. The torque on the electron from a constant magnetic field is simply

$$T = \mu_e H \sin(\theta)$$

By comparison with the above result for a spinning top, it is obvious that the precessional frequency is simply given as

$$\omega_0 = \gamma H$$

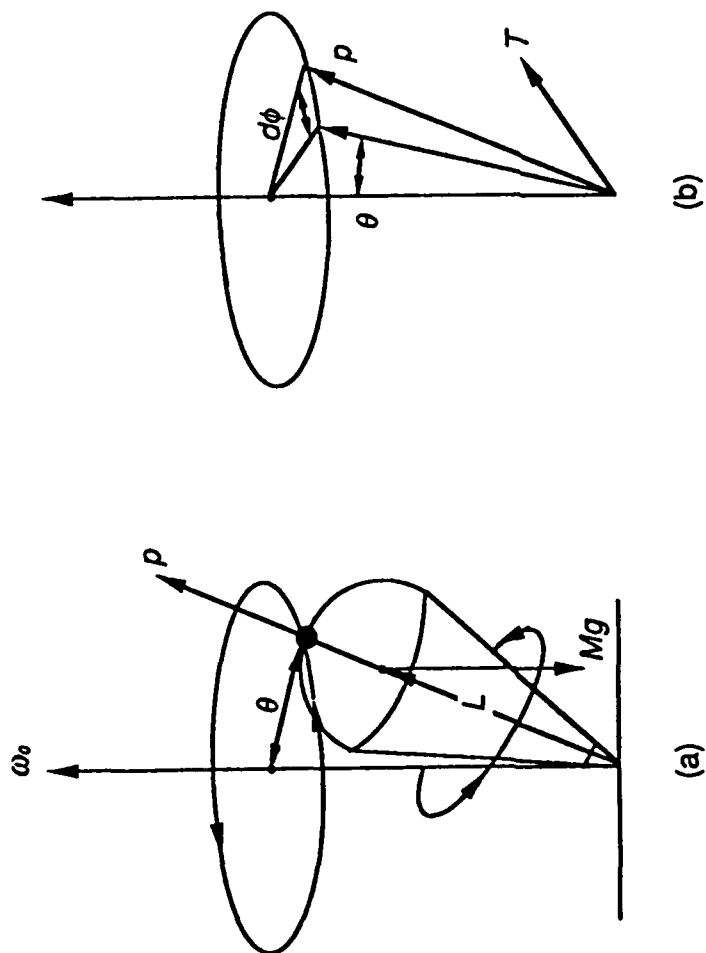


Figure 9: Precessional motion of a spinning symmetrical top in a gravitational field. The precession of the rigid body at frequency ω_0 is shown schematically in (a), and the angular momentum and torque vectors are shown in (b).

Here the magnetic field H is the actual magnetic field seen by the electron and represents the vector sum of both the internal and applied external fields.

In the case of microwave circulators a very large external field is applied which dominates the internal fields. In this case the resonance line width is very narrow and occurs at thousands of megahertz. In the cases where the internal field dominates, the resonance occurs at much lower frequencies and the line width is quite broad as the internal domain structure is by definition nonisotropic and is randomly oriented with respect to the applied field. The internal field arises from the alignment of individual spinning electrons into domains and is given by

$$H_{int} = M_{sat}/(\mu - 1)$$

If the alignment is truly random then a simple vector sum will result in an average field given as

$$H_{int} = 2/3 M_{sat}/(\mu - 1)$$

Therefore, as related above, the resonant frequency in the absence of an externally applied field is given by:

$$\nu_{res} = \frac{\gamma \cdot M_{sat}}{3 \cdot \pi \cdot (\mu_i - 1)}$$

where:

γ = gyromagnetic ratio ($\sim 0.22 \times 10^6$)

M_{sat} = Saturation magnetization ($2.5 \rightarrow 3.5 \times 10^5$ A/M)

μ_i = Initial permeability as $\nu \rightarrow 0$.

It is now obvious that the resonant frequency of a material can be easily shifted through a variety of measures. Application of an external bias field parallel to the applied time dependent field will increase the resonant frequency. Annealing a toroidal ferrite in the presence of a strong toroidal field can increase the ferromagnetic resonant frequency by a factor of 1.5. Reduction of the permeability will also increase the resonant frequency. This can be accomplished through the introduction of an air gap in the toroid or through a change in composition.

C2025, C2050, C2075, N40 High Frequency Nickel-Zinc Ferrites

This group of materials was specifically engineered to give high flexibility in accommodating requirements to 400 MHz. Our engineering department will work with you on your particular needs to determine which if these ferrites is best for you.

Typical Magnetic Characteristics

	C2025	C2050	C2075	N40
INITIAL PERMEABILITY, <1 MHz	175	100	35	15
MAXIMUM PERMEABILITY	1100	390	150	50
MAXIMUM FLUX DENSITY, 'gaus	3500	3400	2700	1600
REMANENT FLUX DENSITY, 'gaus	2600	2400	1800	700
COERCIVE FORCE, 'cerstad	1.5	3.0	7.0	7.5
CURIE TEMPERATURE, °C	270	340	420	510
dc VOLUME RESISTIVITY, ohm-cm	10^6	10^7	10^8	10^{10}
'@ 40 cerstad applied field strength				

Initial Permeability Versus Frequency

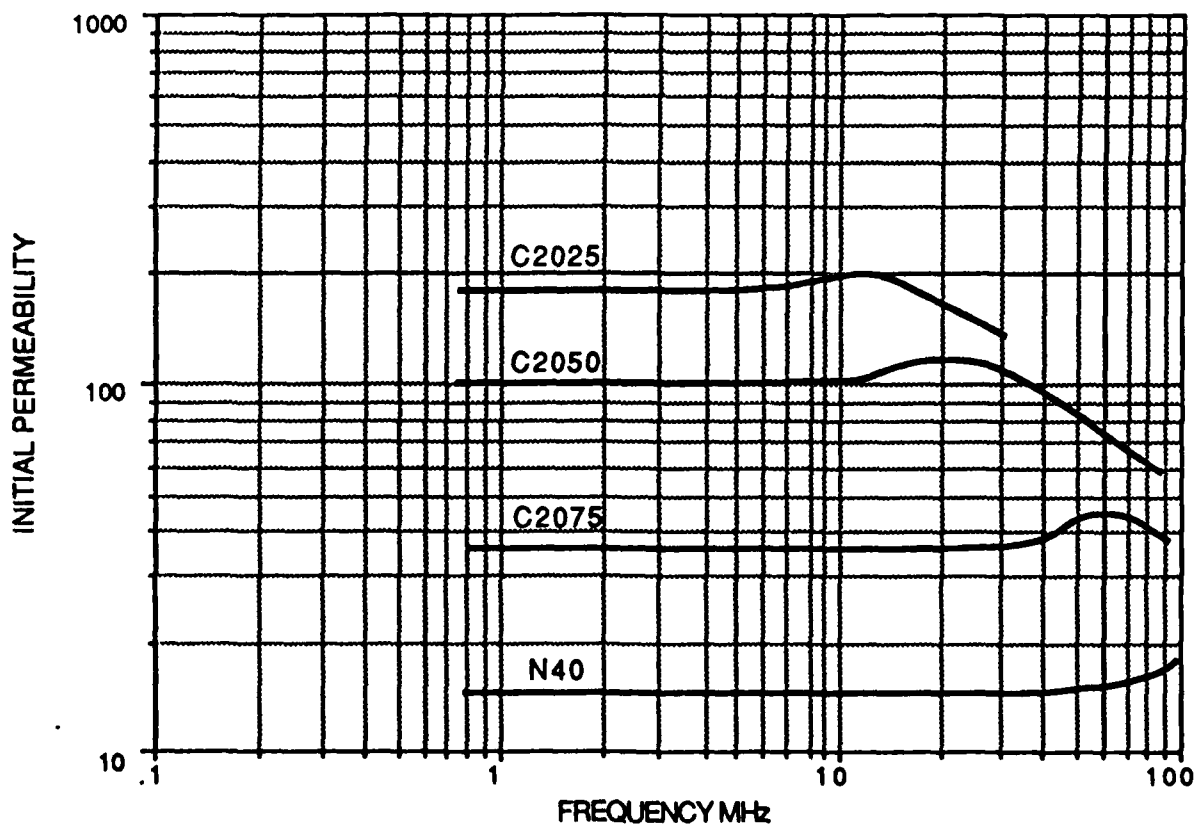


Figure 10: Real part of the initial permeability as a function of frequency for various ferrite materials

In zinc-nickel ferrites the initial permeability and therefore the ferrimagnetic resonant frequency can be varied simply by reducing the zinc content and replacing it with additional nickel. An example of this behavior is shown in a plot of the real part of the initial permeability versus frequency for ferrites of various compositions shown in Fig. 10. These ferrites are manufactured by Ceramic Magnetics Corporation and the compositions $(\text{Zn}_{45} \text{Ni}_{55})$, $(\text{Zn}_{30} \text{Ni}_{70})$, $(\text{Zn}_{15} \cdot \text{Ni}_{85})$, $(\text{Ni}_{1.0}) \cdot \text{Fe}_2\text{O}_4$ correspond to C2025, C2050, C2075, N40 respectively. Also available from this manufacturer are the compositions $(\text{Zn}_{54} \text{Ni}_{46})$, $(\text{Zn}_{60} \text{Ni}_{40})$, $(\text{Zn}_{65} \text{Ni}_{35}) \cdot \text{Fe}_2\text{O}_4$ corresponding to C2010, CN20, and CMD5005 respectively. These ferrites were chosen as test candidates and samples were purchased. Preliminary evaluation eliminated both C2075 and N40 from consideration. These ferrites are only suitable to applications as transformer cores at frequencies in excess of 50 MHz.

It is also critical to note that as the initial permeability drops, the Curie temperature increases. This can be understood by realizing that as the permeability drops, the energy required to change magnetic states increases and therefore the random thermal energy required to disrupt the state also increases. If a ferrite, close to its ferrimagnetic resonance as is the case with the ATA accelerator at LLNL, is replaced by a new composition having a higher nickel content, not only will the losses be reduced but the allowed power dissipation for a given cooling rate will also increase due to the increased Curie temperature. The proper choice of ferrite for use in the accelerator cells is critical, since cell cooling will limit performance as the accelerator repetition rate is increased to provide high average power.

Dielectric Properties

Ferrites are semiconductors with resistivities ranging from $10 \Omega \text{ cm}$ to $10^8 \Omega \text{ cm}$ at room temperature. The dielectric permittivity ranges from 10 to as high as 100,000. The dielectric permittivity along with its frequency dependence are extremely important parameters in induction cell design as the ferrite forms the transmission line media.

Ferrite is a polycrystalline material consisting of semiconducting grains surrounded by thin boundaries with much higher resistivity. The grain boundaries are typically composed of in-

soluble materials which diffuse to the grain boundaries during sintering. They are typically nonmagnetic and are occasionally added intentionally. Calcium Oxide and Silicon Dioxide are examples of materials which are sometimes added by the manufacturer to increase the low frequency resistivity. One example of such a material is Ceramic Magnetics MN8CX. This ferrite is a manganese-zinc ferrite with an artificially high DC resistivity 10,000 Ωcm . As we will see below, such additions are of little practical significance at high frequencies where the large capacitance of these grain boundaries shunts the high resistivity, exposing the inherent resistivity of the crystallites.

If we define α as the ratio of the boundary layer thickness to thickness of the average crystallite, then we can predict the dielectric behaviour of the ferrite based on the following experimentally determined conditions: $\alpha \ll 1$, $\epsilon_{\text{crystallite}} \approx \epsilon_{\text{boundary}}$, and $\alpha \rho_{\text{boundary}} \gg \rho_{\text{crystallite}}$. Therefore at low frequencies the impedance of the crystallite is negligible compared to the impedance of the boundary layers and the resistivity is approximately given as $\alpha \rho_{\text{boundary}}$ and the permittivity approaches $\epsilon_{\text{boundary}}/\alpha$.

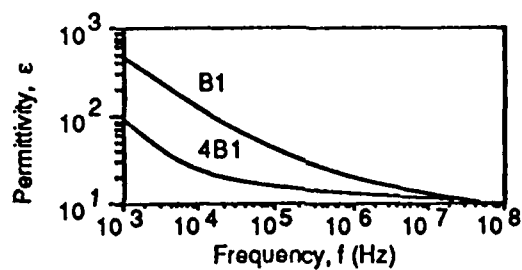
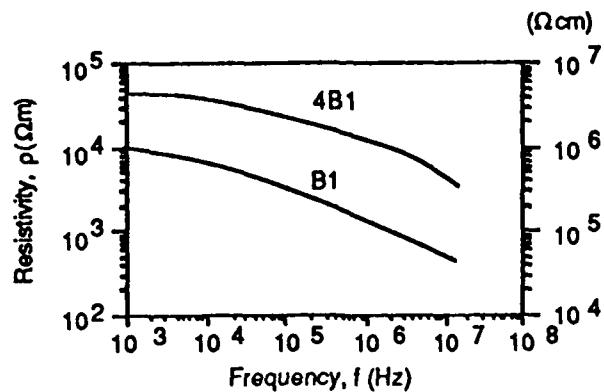
At high frequencies the boundary layer capacitance is short circuited by the high boundary layer capacitance and the dielectric permittivity and resistivity approach that of the crystallites. The relaxation frequency is defined as $1/2\pi\tau$ where τ is the characteristic decay time of the junction capacitance. The relaxation frequency is given by

$$f_r = \frac{1}{2\pi\epsilon_0} \frac{\frac{1}{\rho_{\text{crystallite}}} + \frac{1}{\rho_{\text{boundary}}}}{\epsilon_{\text{crystallite}} + \epsilon_{\text{boundary}}/\alpha}$$

Experimentally-measured curves of both permittivity and resistivity as a function of frequency for two different zinc-nickel compositions are presented in Fig. 11. These compositions labeled B1 and 4B1 are produced by Phillips and correspond to $(\text{Zn}_{60} \text{Ni}_{40})$ and $(\text{Zn}_{50} \text{Ni}_{50}) \cdot \text{Fe}_2\text{O}_4$ respectively.

The eddy current power loss density is simply given as

$$P = \frac{(\omega B_0 d)^2}{\rho \beta}$$



	Code No.	Manufr.	Class
NiZn ferrite	B1	4	VI
	4B1	4	VII

Figure 11: Experimentally-measured permittivity and resistivity for two zinc-nickel compositions

where ρ is the resistivity, d is the characteristic dimension and β is the geometric factor. For a toroid, d is the width of the toroid and $\beta = 24$. For a sphere d is the diameter and $\beta = 80$. The eddy current losses can also be characterized as a contribution to the loss angle given as

$$\tan \delta_r = \frac{\omega \mu \mu_0 d^2}{2 \rho \beta}$$

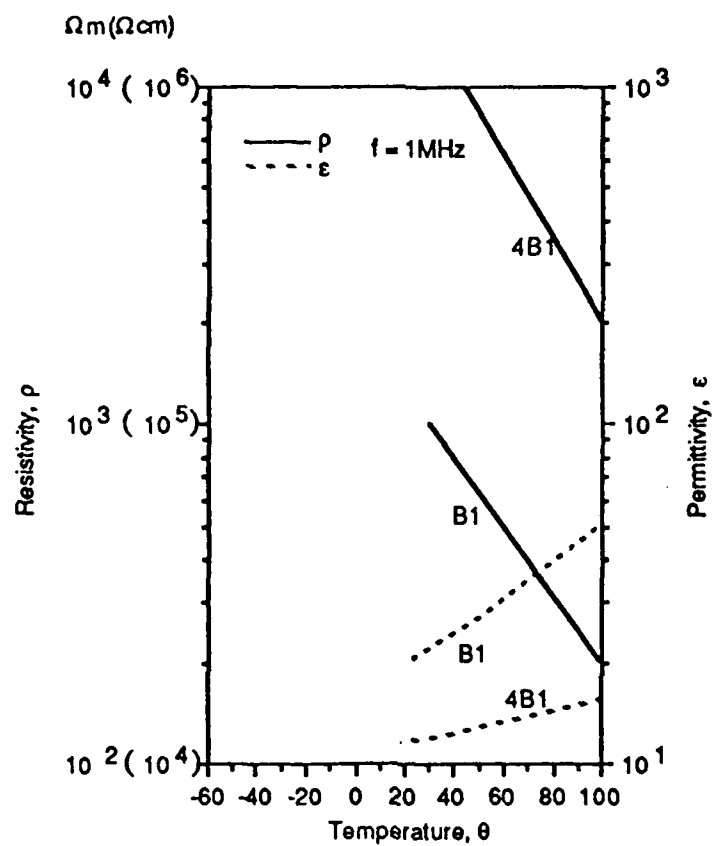
The resistivity and permittivity are also temperature dependent. This effect is documented by the measurements presented in Fig. 12 for the same two compositions. These measurements were taken at 1 MHz but the slopes of the curves are similar at differing frequencies.

The curves indicate that for Zn-Ni compositions, the resistivity never will drop below $10^4 \Omega\text{cm}$. This resistivity is 10^8 times higher than the resistivity of metglass. The eddy current losses in a 1-inch-thick Zn-Ni toroid are equivalent to the losses in a 0.1 mil metglass tape for the same flux excursion. In Mn-Zn ferrites, the eddy current losses cannot be neglected as the resistivity approaches $10 \Omega\text{cm}$ in the frequency range of interest. This means that a 1 inch thick Mn-Zn ferrite toroid will exhibit eddy current losses equivalent to 3 mil thick metglass tape undergoing the same flux excursion. In addition, the Mn-Zn ferrites exhibit a large dielectric constant. Electromagnetic radiation propagates through the material at only a few centimeters per microsecond. This allows fairly small structures to be resonant at the frequency ranges we are interested in. If the entire ferrite toroid forms a single resonant structure, the loss tangent approaches unity.

2.4 Ferrite Sample Measurements

In the Phase I effort, sample ferrites were purchased which spanned the range of applicable compositions. These ferrites were manufactured by Ceramic Magnetics Corporation and the compositions purchased $(\text{Zn}_{65} \text{Ni}_{35})$, $(\text{Zn}_{60} \text{Ni}_{40})$, $(\text{Zn}_{54} \text{Ni}_{46})$, $(\text{Zn}_{45} \text{Ni}_{55})$, $(\text{Zn}_{30} \text{Ni}_{70})$, $(\text{Zn}_{15} \text{Ni}_{85})$, $(\text{Ni}_{1.0}) \cdot \text{Fe}_2\text{O}_4$ correspond to CMD-5005, CN20, C2010, C2025, C2050, C2075, N40 respectively. Preliminary evaluation eliminated both C2075 and N40 from consideration. These ferrites are only suitable to applications as transformer cores at frequencies in excess of 50 MHz.

A test stand was assembled to evaluate the samples. The simplified schematic of the test stand is presented in Fig. 13. Samples were reset slowly and then rapidly cycled from $-B_r$ to B_r .



	Code No.	Manufr.	Class
NiZn ferrite	B1	4	VI
	4B1	4	VII

Figure 12: Temperature dependence of the permittivity and resistivity of two zinc-nickel compositions

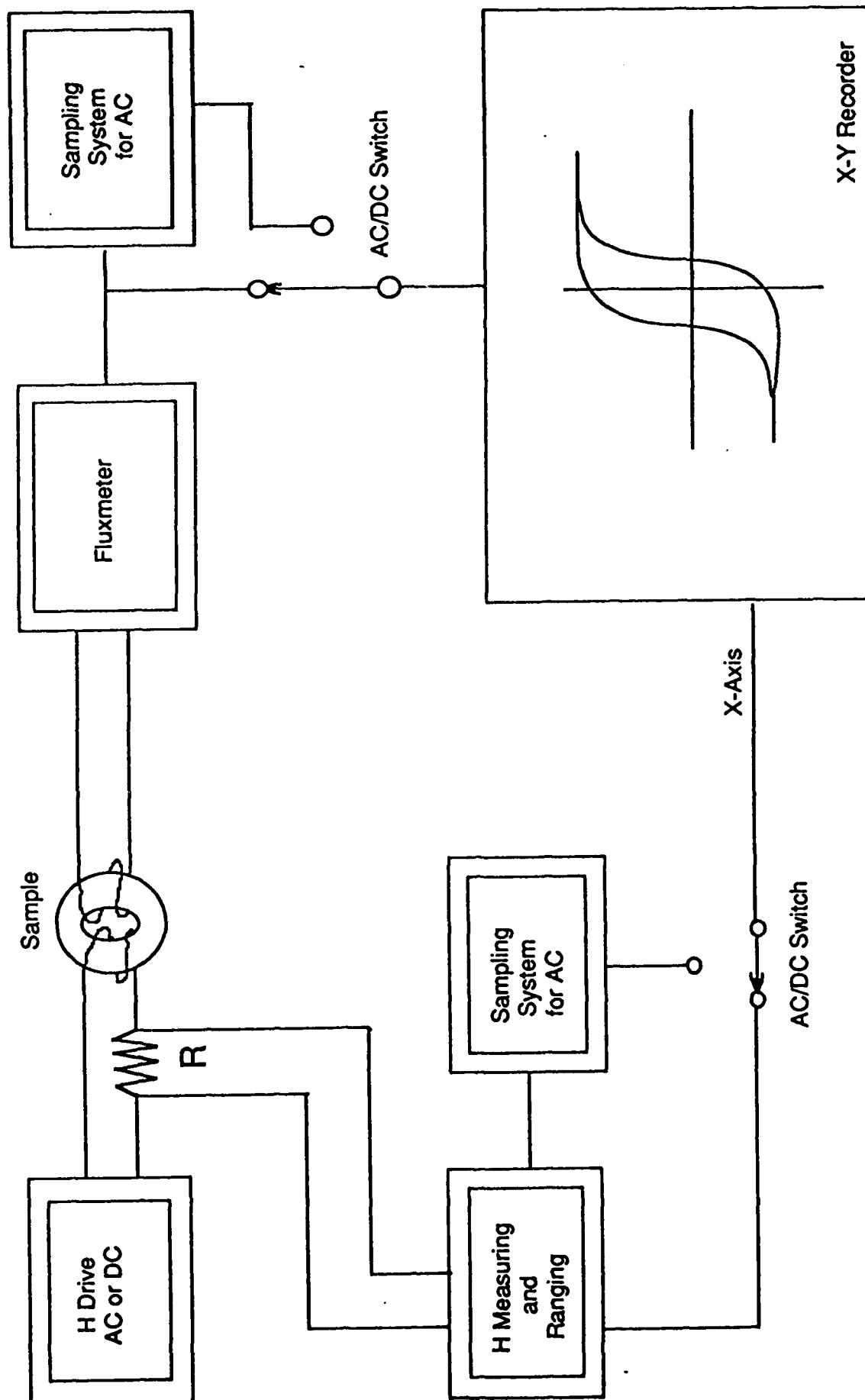


Figure 13: B-H loop measurements

Minor loops were not measured as they are not of interest in the applications we are considering where all of the ferrite's available flux excursion is typically required. The saturation time scales of interest range from 50ns to 500ns. At saturation times longer than 500ns, metal tape wound cores will outperform any available ferrite. At saturation times shorter than 50ns, Zn-Ni ferrites are typically replaced by ferrites containing magnesium, titanium and cobalt. The experimental results are presented in Figs. 14-17.

The energy dissipated in the ferrite as the flux swings from $-B_s$ to B_s , which is simply the area enclosed by the hysteresis loops in the B-H plane is plotted as a function of saturation time in Fig. 18. The units are Joules/Meter³ versus saturation time in nanoseconds.

If the ferrite is employed as a saturable reactor in a nonlinear magnetic compressor then the volume of core required is linearly dependent on the square of the available flux swing. Simply because a candidate material exhibits a lower loss per unit volume does not mean it is the best choice as the core material. The best technique to identify the optimum core material in a saturable reactor is to plot energy loss per meter³ per Tesla². This plot appears in Fig. 19.

In high repetition rate applications, temperature rise can be a major limitation. As the temperature rises, the available flux swing is reduced until at the Curie temperature the available flux swing ΔB goes to zero. The higher the Curie temperature for a given composition, the more power can be dissipated in a given size sample with a specified surface temperature. In a case where the ferrite surface is anchored to a temperature of 50°C, the plot in Fig. 20 gives an indication of the maximum repetition rate at which a given composition can be operated. Here the energy loss per cycle is divided by the maximum allowable temperature rise. The lower a curve lies on this plot, the higher the usable repetition rate.

2.5 Cooling of Ferrite Cores

Improvements in the performance envelope of ferrite cores can also be achieved through enhanced ferrite cooling. Coolant rates depend not only on the thermal conductivity and geometric dimensions of the ferrite core but also on the shape of coolant channels and the coolant flow dynamics. Efforts were made to avoid long, wide cooling channels which promote laminar flow

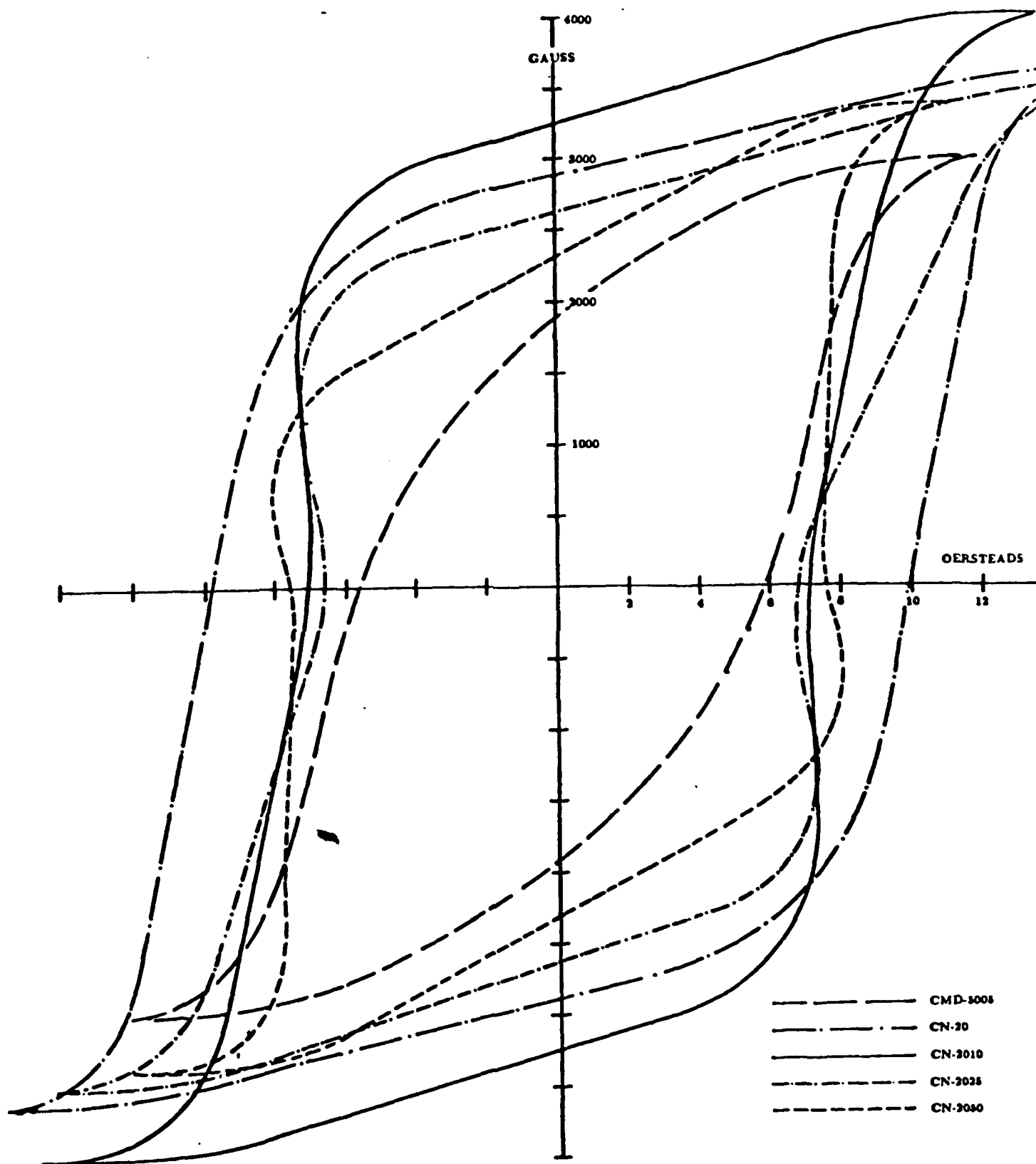


Figure 14: Hysteresis curves for various ferrite materials measured at $\tau_{sat} = 50$ nsec

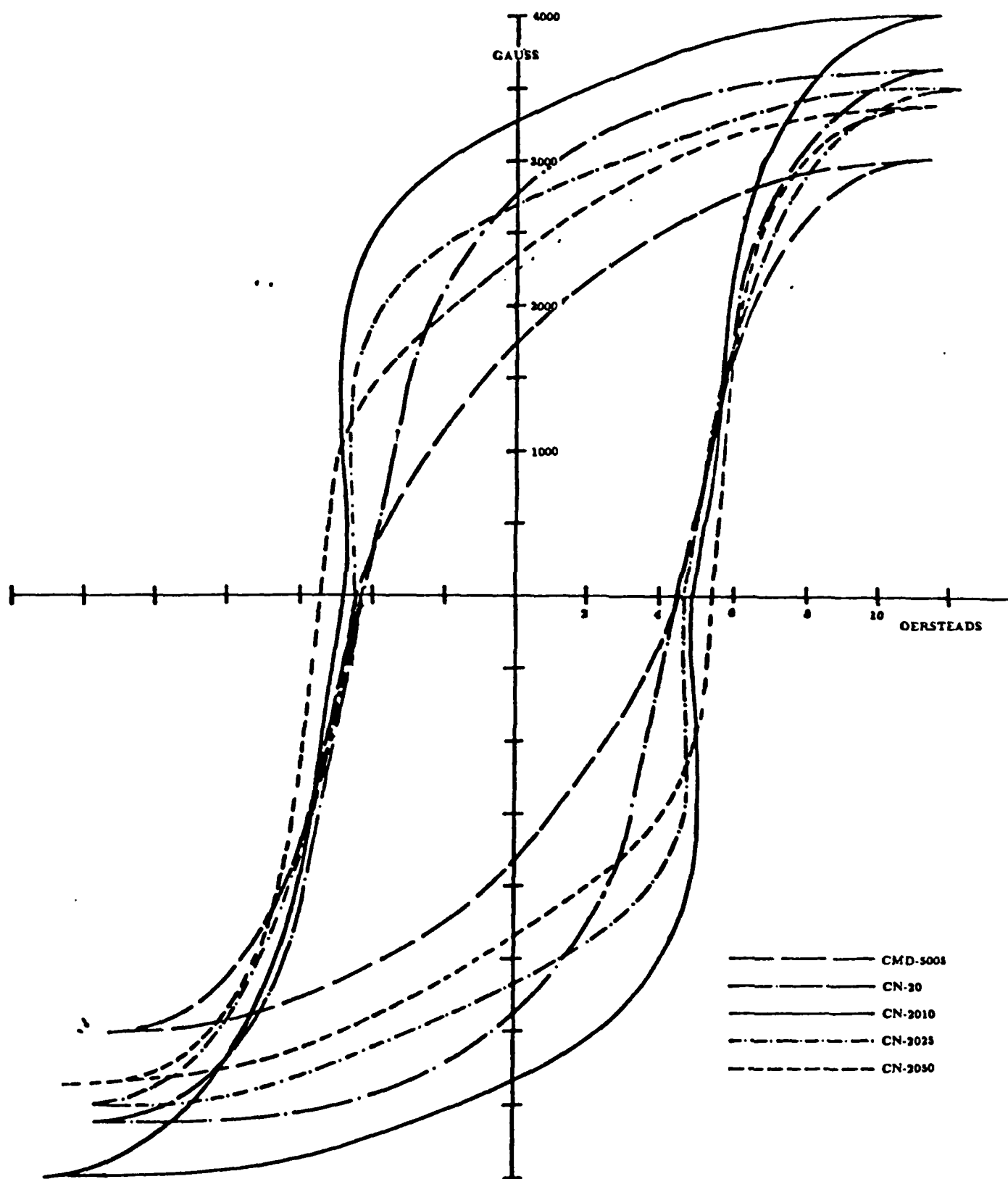


Figure 15: Hysteresis curves for various ferrite materials measured at $\tau_{sat} = 100$ nsec

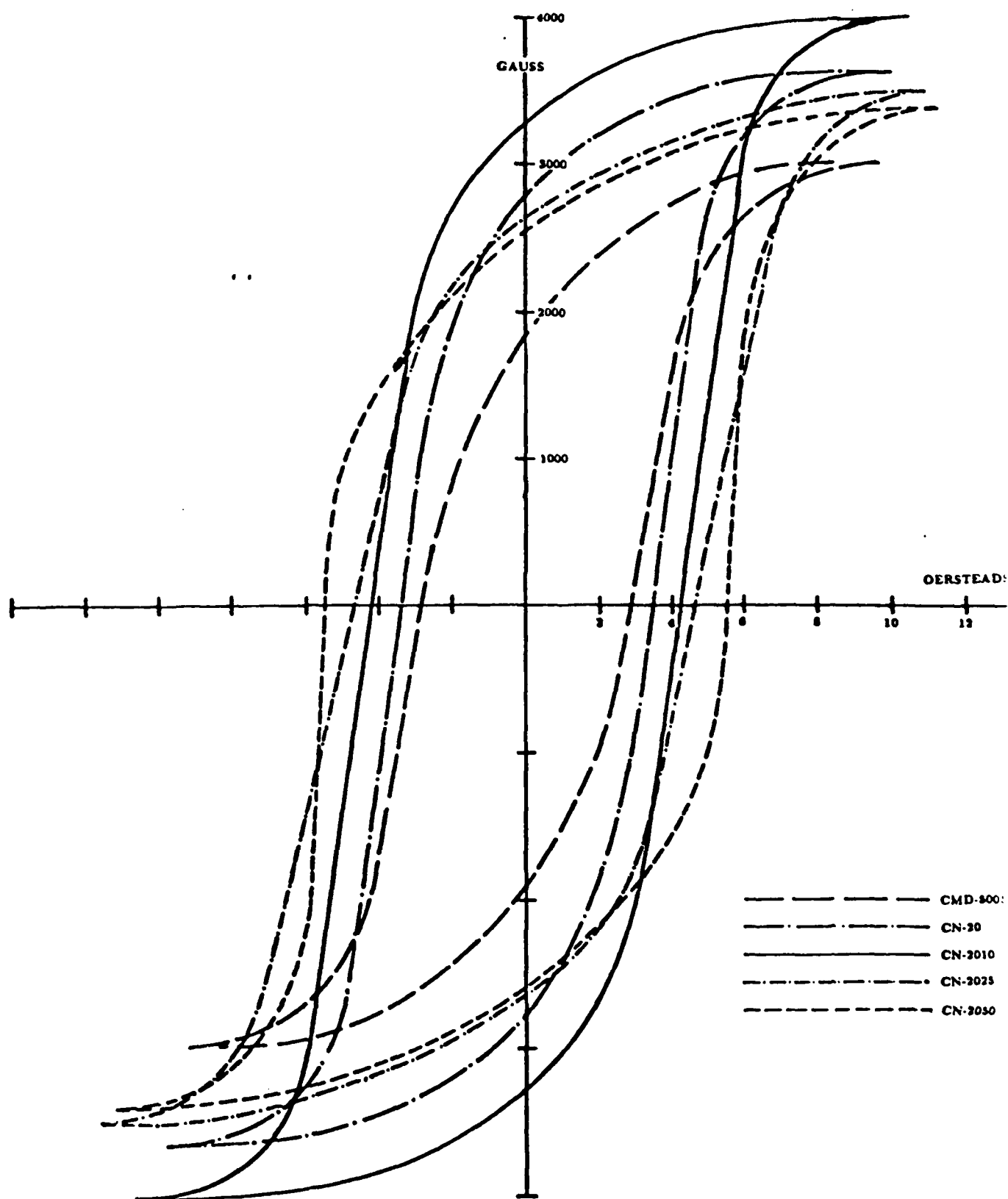


Figure 16: Hysteresis curves for various ferrite materials measured at $\tau_{sat} = 250$ nsec

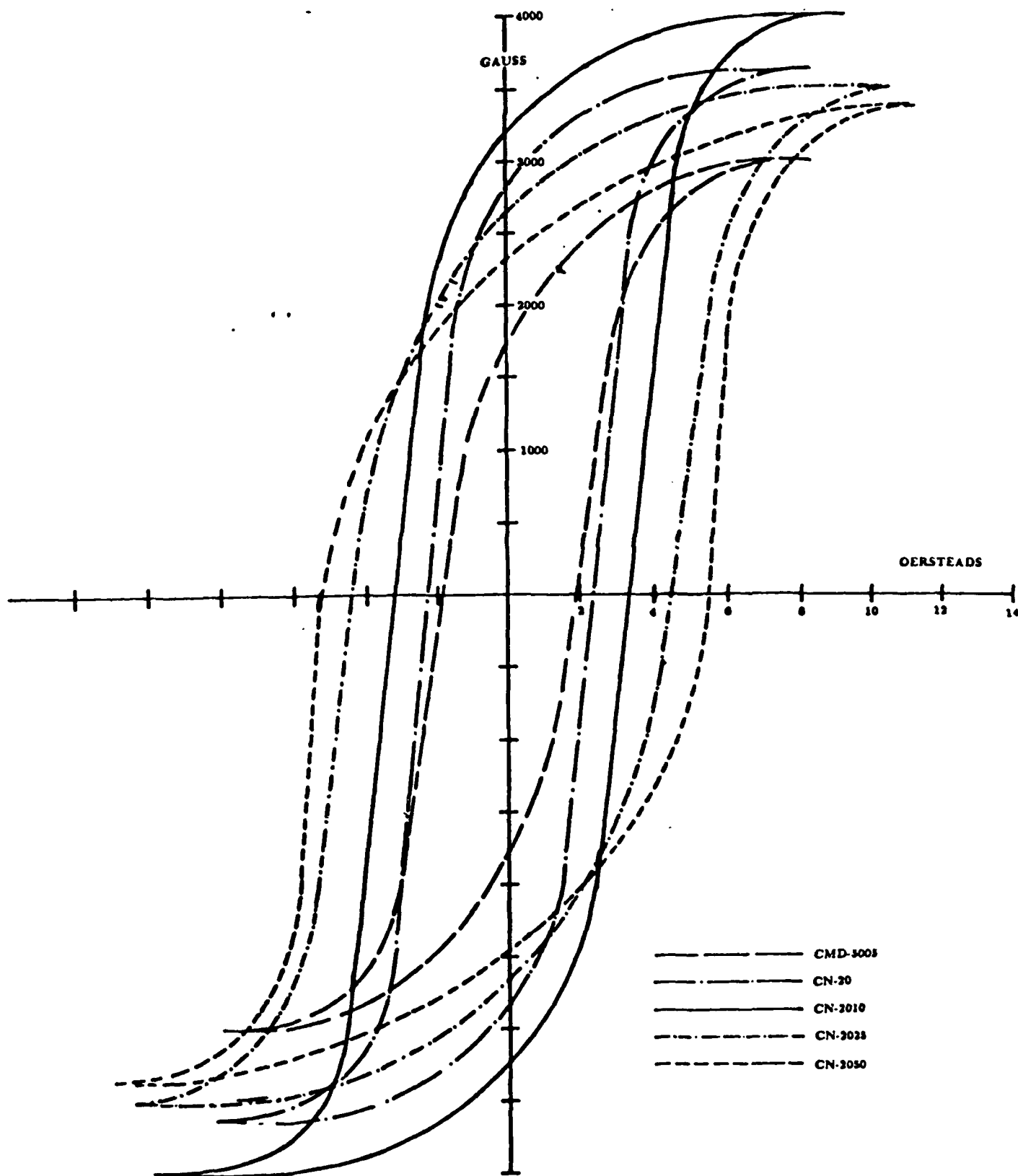


Figure 17: Hysteresis curves for various ferrite materials measured at $\tau_{\text{eff}} = 500$ nsec

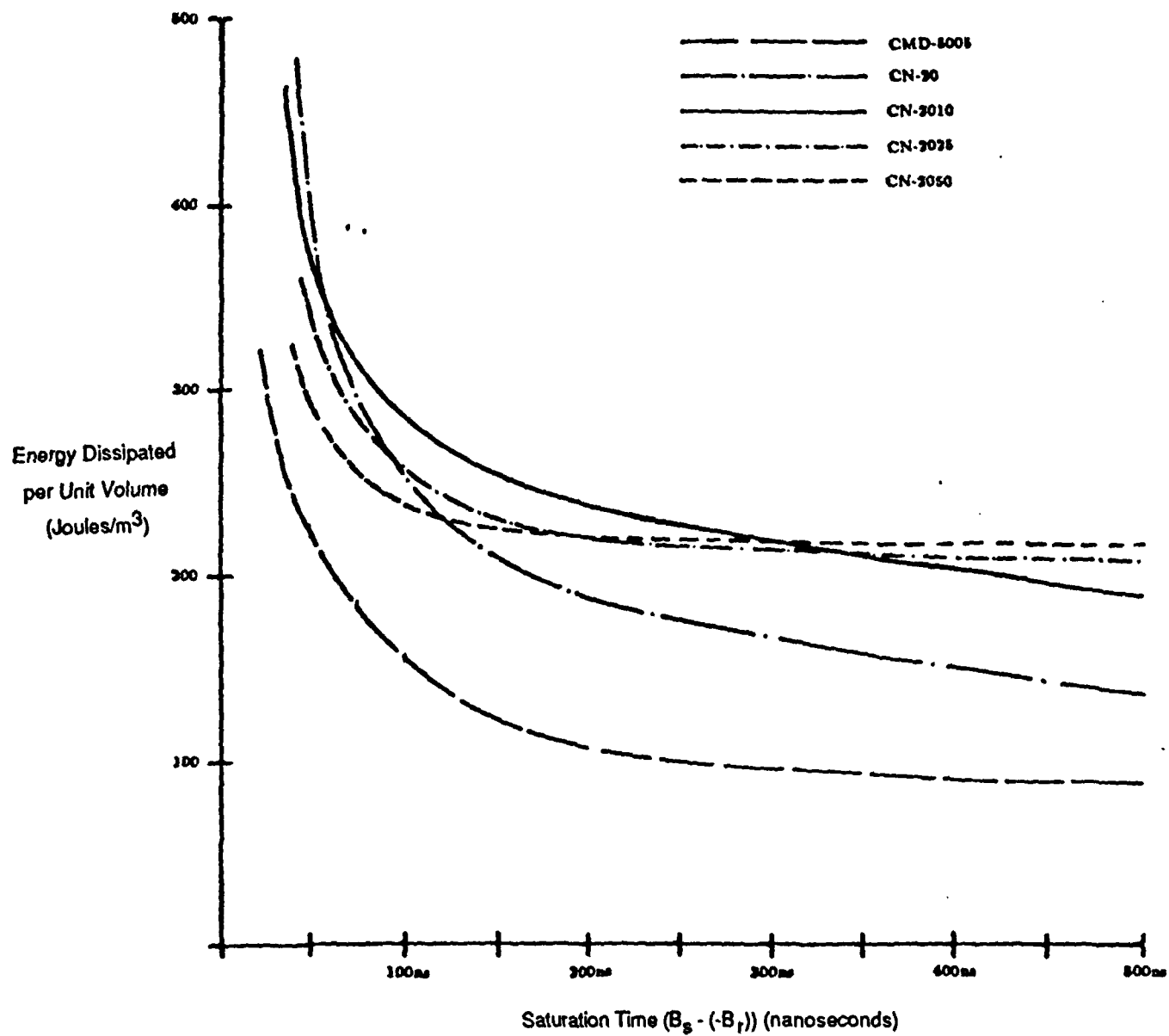


Figure 18: Energy dissipated per unit volume as the flux swings between $-B_r$ and B_s versus Saturation Time

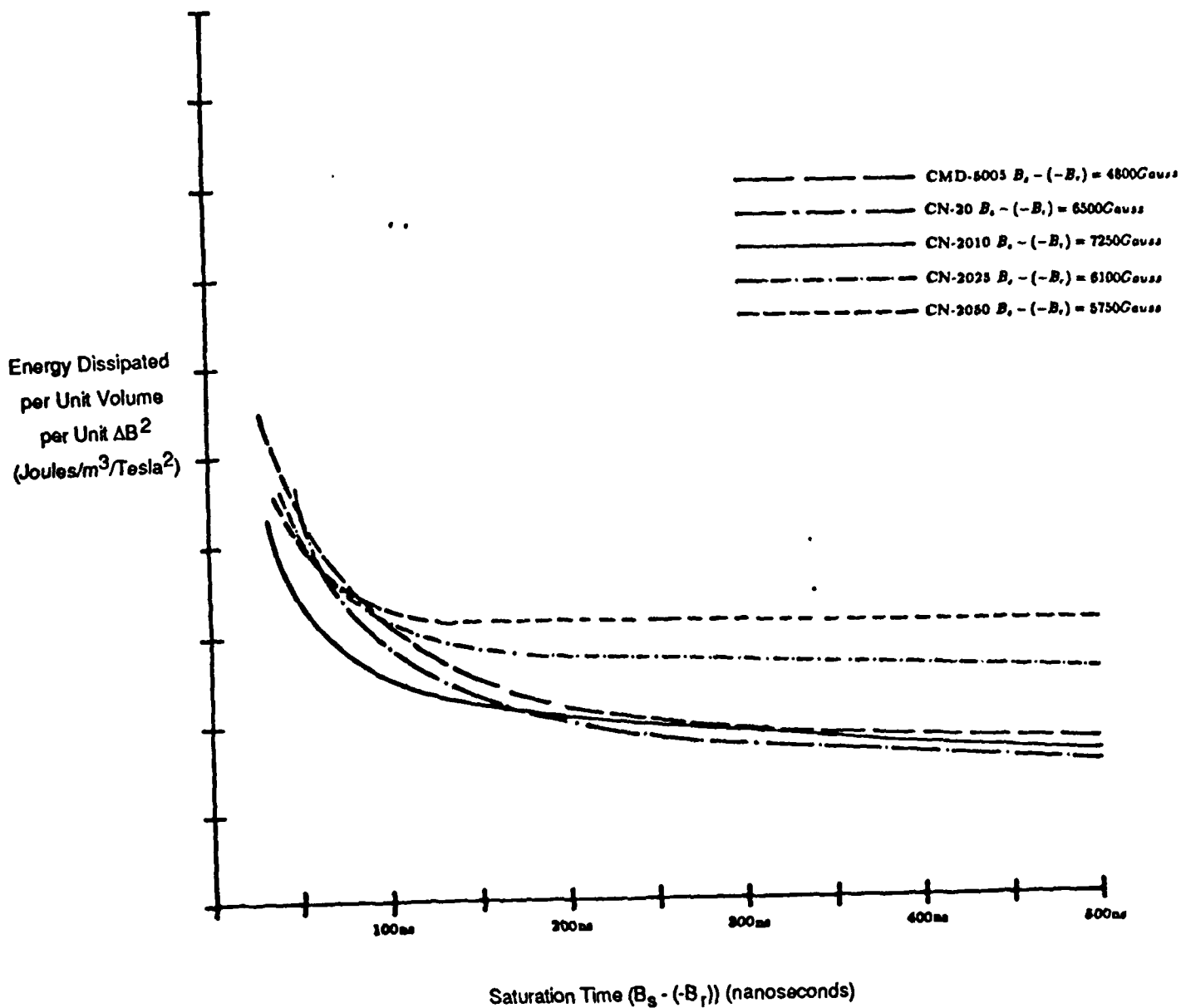


Figure 19: Energy dissipated per unit volume divided by ΔB^2 in Tesla versus Saturation Time

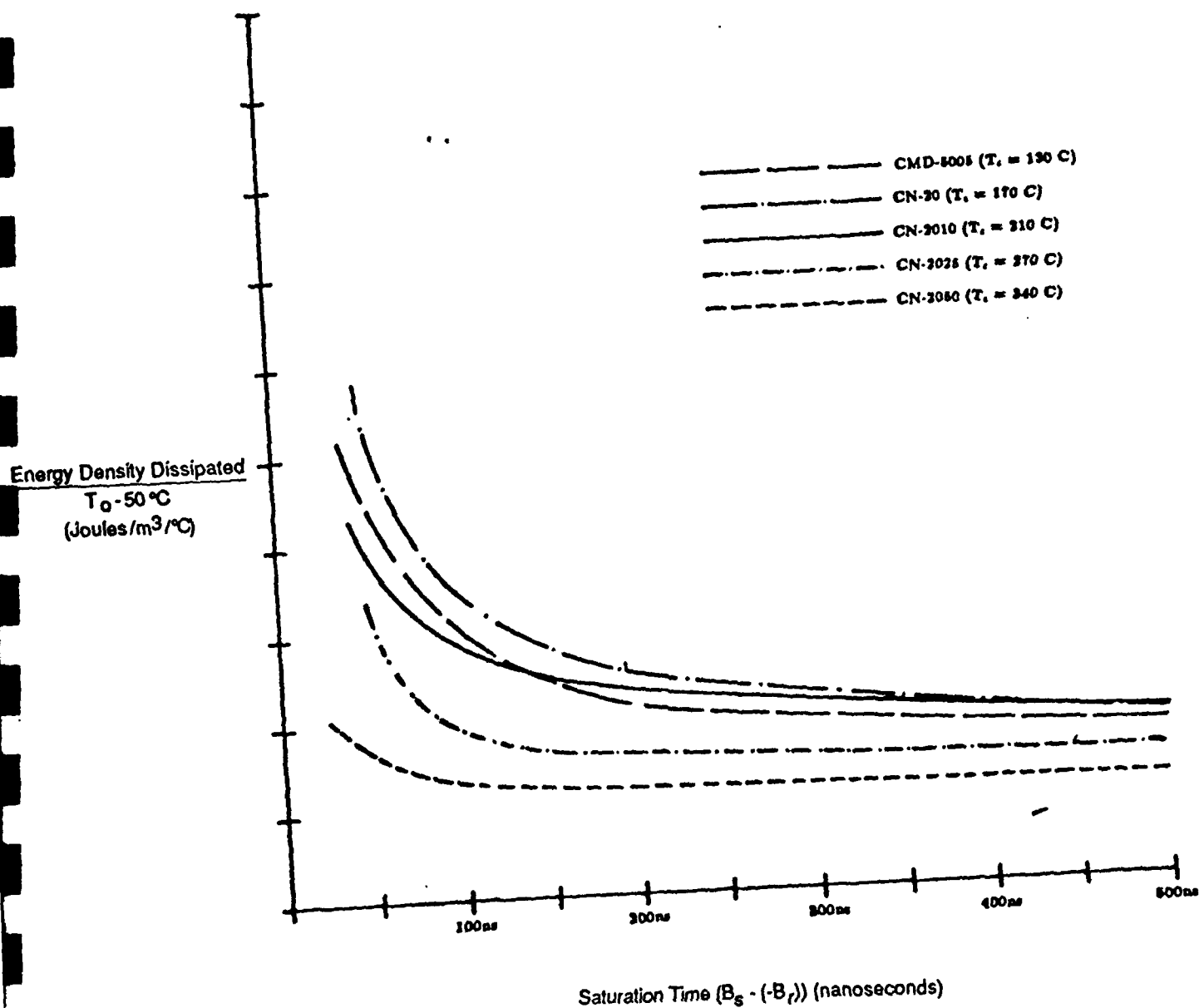


Figure 20: Energy dissipated per unit volume divided by ΔT versus Saturation Time

and reduce the heat transfer coefficients. Short narrow channels are optimum and were broken up at regular intervals to promote turbulence. A coolant liquid with an appropriately selected boiling point and enthalpy is also important as subcooled nucleation can play a critical role in increasing turbulence at the surface.

The heat transfer coefficient of a surface is a strong function of both the geometry and the surface texture. Every effort should be made to break up laminar flow profiles and promote turbulence without causing deterioration of the electrical properties of the ferrite. With an azimuthal magnetic field, radial grooving must be avoided but slotting along a radius can be extremely effective in promoting cooling. By machining slots into the ferrite comprising the multiple coaxial segments, the resistance to fracturing due to differential thermal expansion can also be avoided. Staggering these slots from one toroid to the next will break up the laminar flow patterns and promote turbulence.

The accelerator cell ferrite must be maintained at a temperature well below its Curie point. Energy is dissipated in the core material at a rate of ~ 300 joules/m³ per pulse. Waste heat removal is expedited by segmenting the core into thin split-washer-like toroids. The ferrite is immersed in freon and is cooled by the enthalpy of vaporization. In the case of the accelerator cell design discussed above, the ferrite is not allowed to saturate and the average energy deposition is only 150 joules/m³ per pulse. The core volume of 3.7 liters results in ~ 0.5 joules per pulse per cell waste heat generation. Assuming f-11 Freon is used as a coolant (enthalpy of boiling = 180 joules/gram, vapor density = 0.005 grams/cm³) the boiling rate would be ~ 0.5 cm³/Hz. Bubbles generated through this process proceed up the drive cables into the driver where heat exchangers recondense the vapor back into the liquid phase. This method of cooling eliminates flowing liquids with the exception of room temperature coolant water to supply the heat exchangers. In the event that space or air basing is desired, a recirculating refrigerant might replace the water in the heat exchanger.

The maximum repetition rate at which a ferrite can be operated is determined by its Curie temperature and cooling rate. The cooling rate will depend on the temperature of the coolant,

the temperature drop at the surface, and the temperature drop from the interior to the surface of the ferrite. The largest temperature drop for most geometries of interest is between the surface and the interior of the ferrite. The rate of heat transfer perpendicular to a lamina of area A , thickness δx , and thermal conductivity λ , when the temperature difference is $\delta\theta$, is given by $\lambda A \delta\theta / \delta x$ or

$$P_{cond} = \frac{\lambda \delta\theta}{\delta x} W/cm^2$$

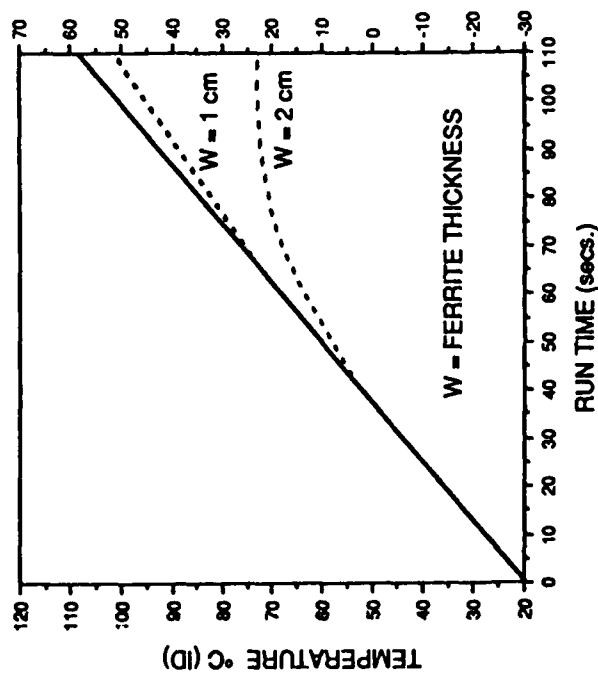
where P_{cond} is the rate of heat transferred by conduction. For a slab of thickness, d , the temperature difference between the center and the surface is given by

$$\Delta\theta = \frac{\text{Power dissipated/Unit Volume}}{8\lambda} \cdot d^2$$

The dimensions are in units of centimeters and degrees Celsius. For zinc-nickel ferrites $\lambda = 4 \cdot 10^{-2} W/cm^2$.

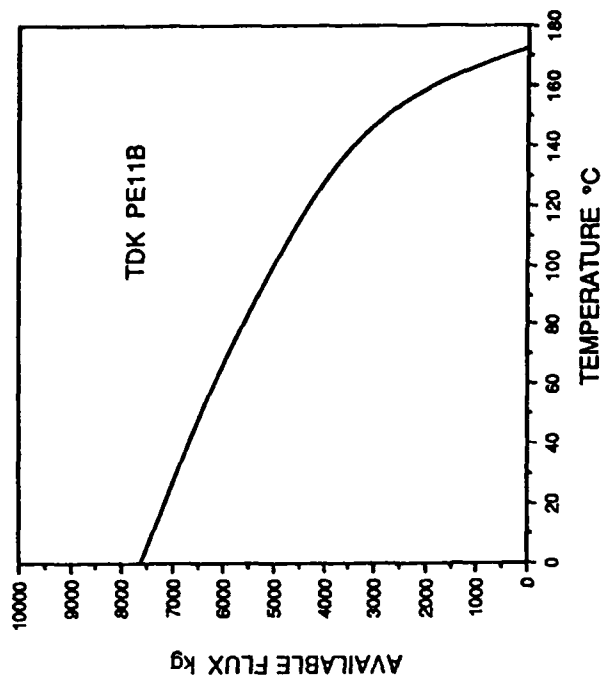
In some applications, the run duration is short enough that it will simplify the design considerably if the ferrite is simply allowed to heat up. As long as the temperature excursion is small compared to the Curie temperature of the material there will be little change in the ferrite performance. The heat capacity of Zinc-Nickel ferrites is $\approx 0.75 J/g^\circ C$. The curve in Fig. 21 illustrates how little is gained by complex measures to cool a ferrite core operating a 10 kHz for 100 seconds. The ferrite in this case is a 60-40 Zinc Nickel ferrite. In practice one would probably choose a ferrite with a higher nickel content and correspondingly higher Curie temperature.

The selection of an optimum coolant liquid is critical to the operation of both the nonlinear magnetic pulse compressors and the accelerator cells. The coolant liquid serves both as an insulating and energy storage medium as well as the heat removal medium. The ability of a liquid to remove heat is dependent on many of the liquid properties. Of primary importance is the compatibility of the liquid with the operating environment. The coolant liquid must be non-corrosive, non-conductive, preferably non-flammable and capable of sustaining the electric field stresses which appear in the driver. In addition to these constraints it is preferred that the



— NO COOLING

--- COOLED WITH REFRIGERANT ASSUMING
 ΔT (INTERFACE) $\leq 20^\circ \text{C}$ AND ΔT (COOLANT)
 $\leq 20^\circ \text{C}$ ALSO ASSUMING SUBCOOLED
 NUCLEATION ENHANCEMENT AND
 TURBULENT FLOW AT 30 GPM/CELL



NOTE: CORES MUST BE SEGMENTED RADially
 HANDLE THERMAL SHOCK FROM
 RADIAL DEPENDENT CORE LOSSES.

Figure 21: Cooling of ferrites used in accelerator cells at a repetition rate of 10^4 pps

liquid remove heat by enthalpy of evaporation so that no active flow mechanism is required and waste heat can be removed by the process of heat piping. This requires that the boiling point of the liquid at reasonable operating pressures lie within the desired operating temperature envelopes. For one or more of the above considerations, the best liquids for heat removal (water, mercury, and alcohol) are eliminated.

If a candidate liquid satisfies the above criteria, then a relative figure of merit can be established by comparing the heat capacity, enthalpy of vaporization, thermal conductivity, inverse viscosity and dielectric strength. Referring to Table I, the critical properties for several candidate coolant liquids are summarized. The properties of water, mercury, and methanol are included for comparison. In order of performance, the author would list the candidates as Freon 11, Freon 113, Fluorinert FC-72 and Fluorinert FC-77. Fluorinert FC-72 is the perfluorinated sister to Freon 113 while Fluorinert FC-87 (which no longer appears in the 3M catalog) is the perfluorinated sister to Freon 11. In comparing Freon to Fluorinert it appears that Fluorinert has a dielectric strength almost 1.3 times higher than Freon but that Freon with its lower viscosity and higher enthalpy can remove heat about twice as fast. Fluorinert does have the advantage that it is considerably more chemically stable and non-hygroscopic. It is much less prone to decompose into an organic acid and to contamination by other organic compounds and will not remove the plasticizers from PVC.

2.6 Using Ferrite to Control Dipole Wake Fields

It is important to recognize that the ferrite in the accelerator cells serves two purposes. It serves the purpose of isolating the input drive pulse from ground and it also acts as an absorber for the high frequency dipole modes.

Considerable effort is typically expended to match the strip line impedance presented by the accelerating gap to the radial line impedance extending into the region of the ferrite. This is done to avoid internal reflections of the electron beam wake field. Once these wake fields reach the ferrite, they are attenuated very rapidly. At the high frequencies (≥ 300 MHz) associated with the TM_{011} dipole mode, the ferrite exhibits an impedance very close to that of free space

Table I:
Properties of Coolants

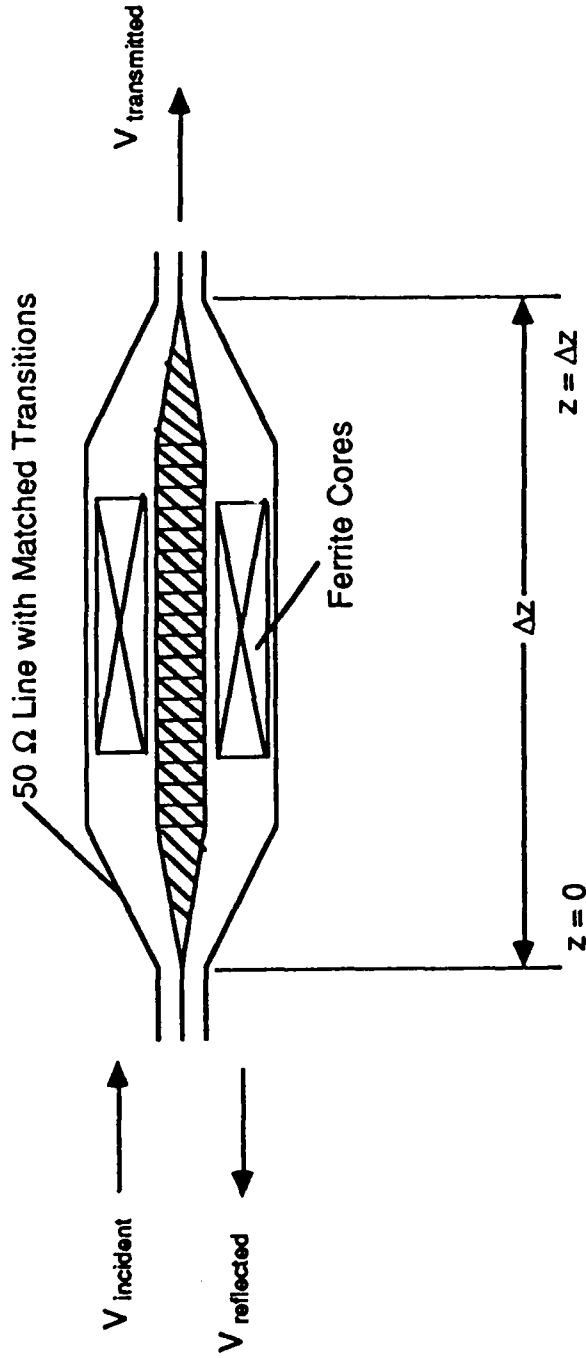
Measurements at 27 °C

Fluid	Thermal Conductivity W/cm - °K	Mass Density kg - m ³	Specific Heat J/kg - °K	Viscosity (m ² /sec)	Enthalpy kJ/kg	Dielectric Strength kV/cm	Relative Dielectric Constant, ϵ_r	Boiling Point °C
Freon 11	0.088	1472	0.888	2.82×10^{-7}	179.2	93		24
Freon 12	0.069	1305	980	1.95×10^{-7}	136.9	72		-29
C ₂ Cl ₃ F ₃ Freon TF 113	0.067	1579	912	4.5×10^{-7}	169	117	1.849	45.8
Methanol	0.2022	785	2534	7×10^{-7}	1179		32.63	65
Water	0.6084	996.6	4177	8.26×10^{-7}	2438		81	100
Mercury	8.34	13,611	139.1	1.2×10^{-7}	302	N/A	∞	356
Fluorinert FC-77	0.064	1730	1044	13.032×10^{-7}	90.29	157		
Fluorinert FC-72	0.057	1680	1044	6.16×10^{-7}	94.8	150	1.76	56

and an attenuation coefficient close to 4 dB/cm. In summary, the ferrite appears as a total absorber for electromagnetic radiation in the frequency spectrum associated with the Beam Breakup Instability.

A test fixture (Fig. 22) was assembled in order to make some measurements of the small field behaviour of ferrite at high frequencies. The two similar compositions tested were TDK PE-11B and STACKPOLE C7D both \approx 60-40 Zn- Ni ferrites. Differing compositions illustrate similar behaviors with the frequency slightly shifted. The results of these measurements can be found in Figs. 23-27.

Ferrite Properties Measurement Technique



2-47

$$V_{\text{inc}} = V_{\text{inc}}(0) e^{-ik_0 z}$$

$$V_r = (1 - \Gamma) V_{\text{inc}}(0) e^{-ik_0 z}$$

$$V_t = \Gamma V_{\text{inc}}(0) e^{ik_0(\Delta z - L_f)} + ik_f L_f$$

$$\therefore (\mu_r \epsilon_r)^{1/2} = 1 + (ik_0 L_f)^{-1} \cdot \ln \left(\frac{V_t(\Delta z)}{\frac{[V_t(\Delta z)]}{V_{\text{inc}}(\Delta z)}} \right)$$

$$\left(\frac{\mu_r}{\epsilon_r} \right)^{1/2} = \frac{1 + \Gamma}{1 - \Gamma}$$

$$\text{Attenuation dB/cm} = \frac{20}{\Delta L_f} \cdot \log \left(\frac{|\Gamma V_{\text{inc}}(\bullet)|}{|V_t(\Delta z)|} \right)$$

Figure 22: Test fixture and design considerations

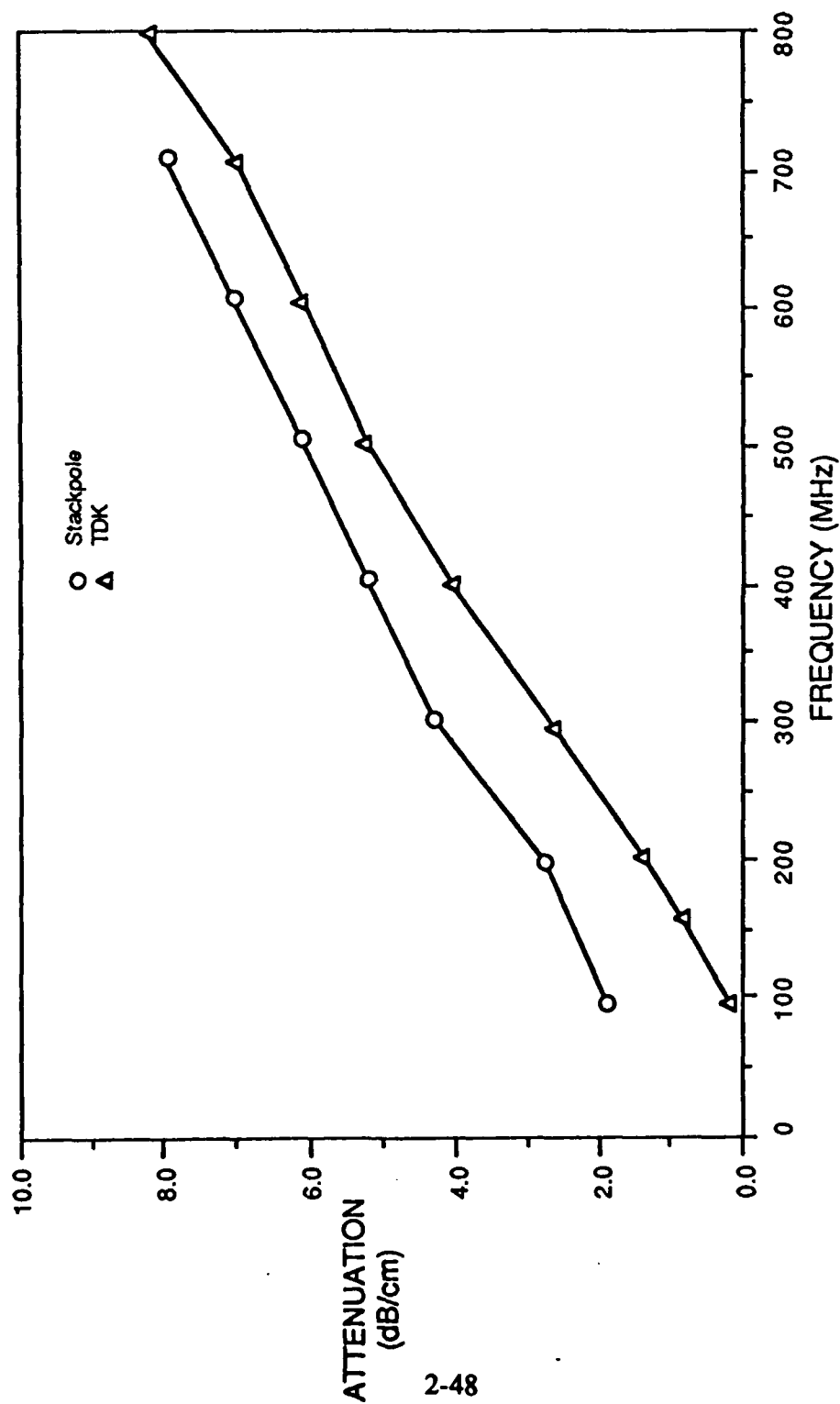


Figure 23: RF attenuation in solid ferrite

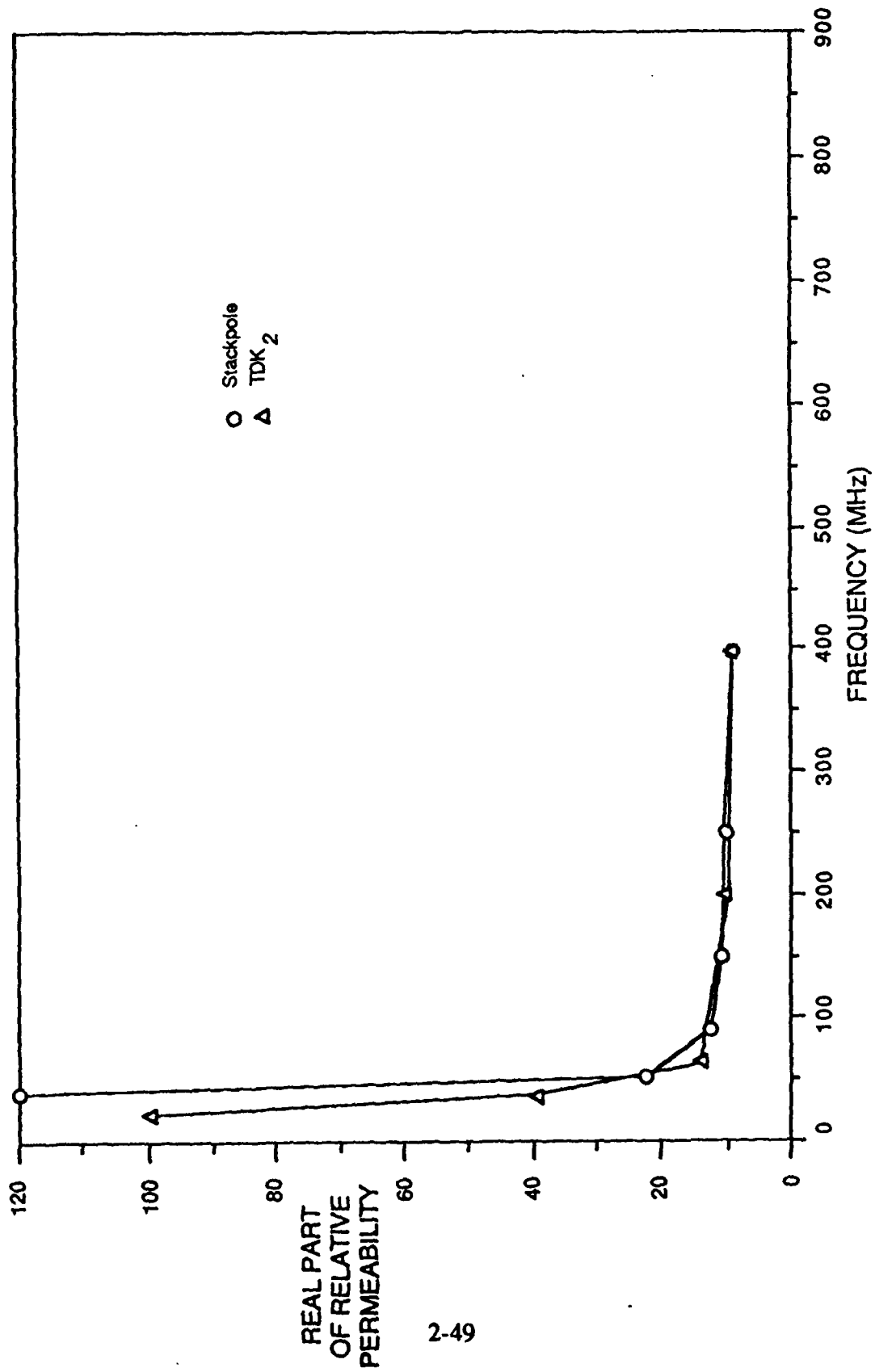


Figure 24: $\text{Re}(\mu_r)$ calculated from $(\mu_r \epsilon_r)^{1/2}$
assuming $\epsilon_r(\omega) = \epsilon_r(\omega = 1 \text{ MHz})$

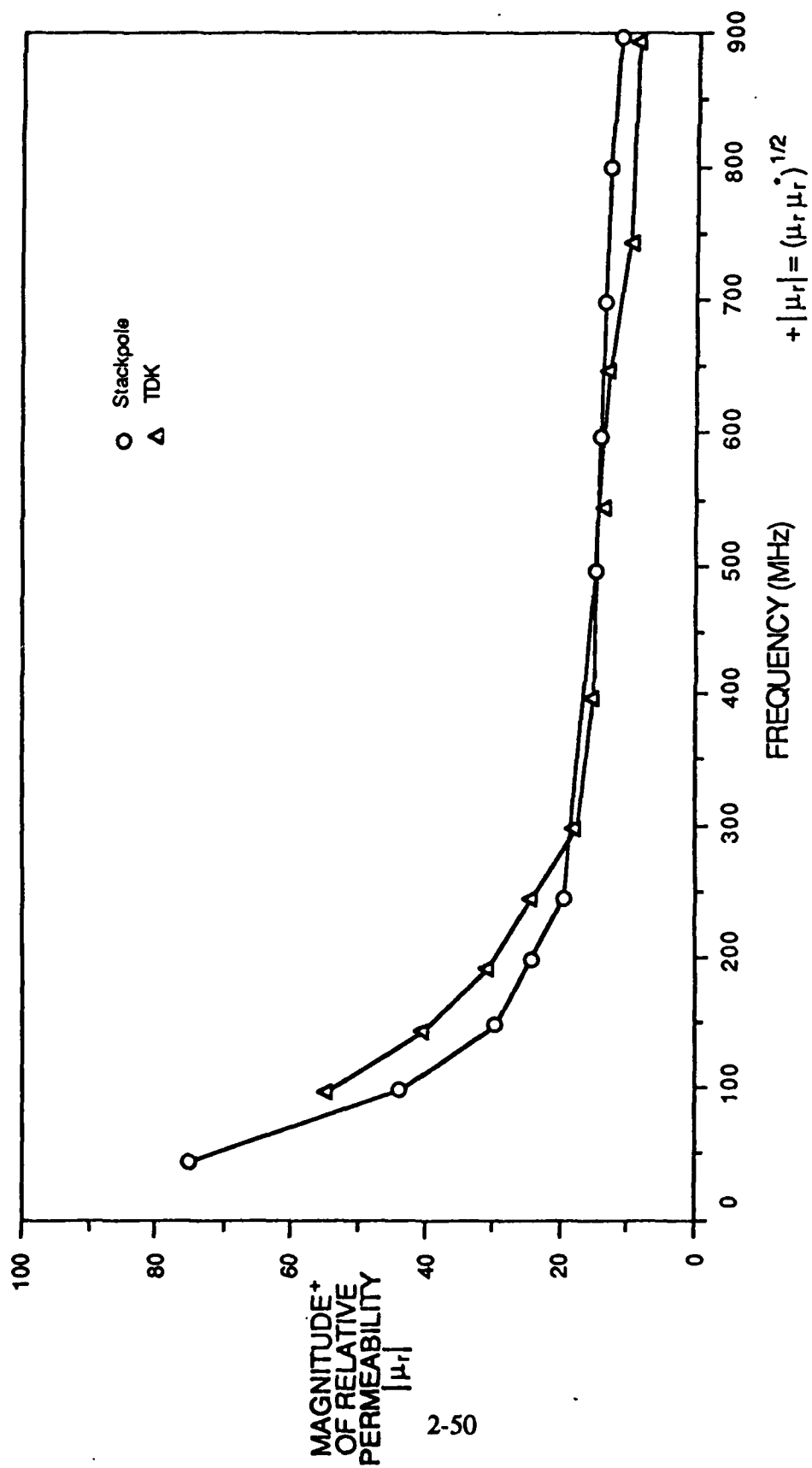


Figure 25: $|\mu_r|^{1/2}$ calculated from $(\mu_r/\epsilon_r)^{1/2}$ and $(\mu_r \epsilon_r)^{1/2}$
assuming $\epsilon_r(\omega) = \epsilon_r|_{1\text{MHz}}$

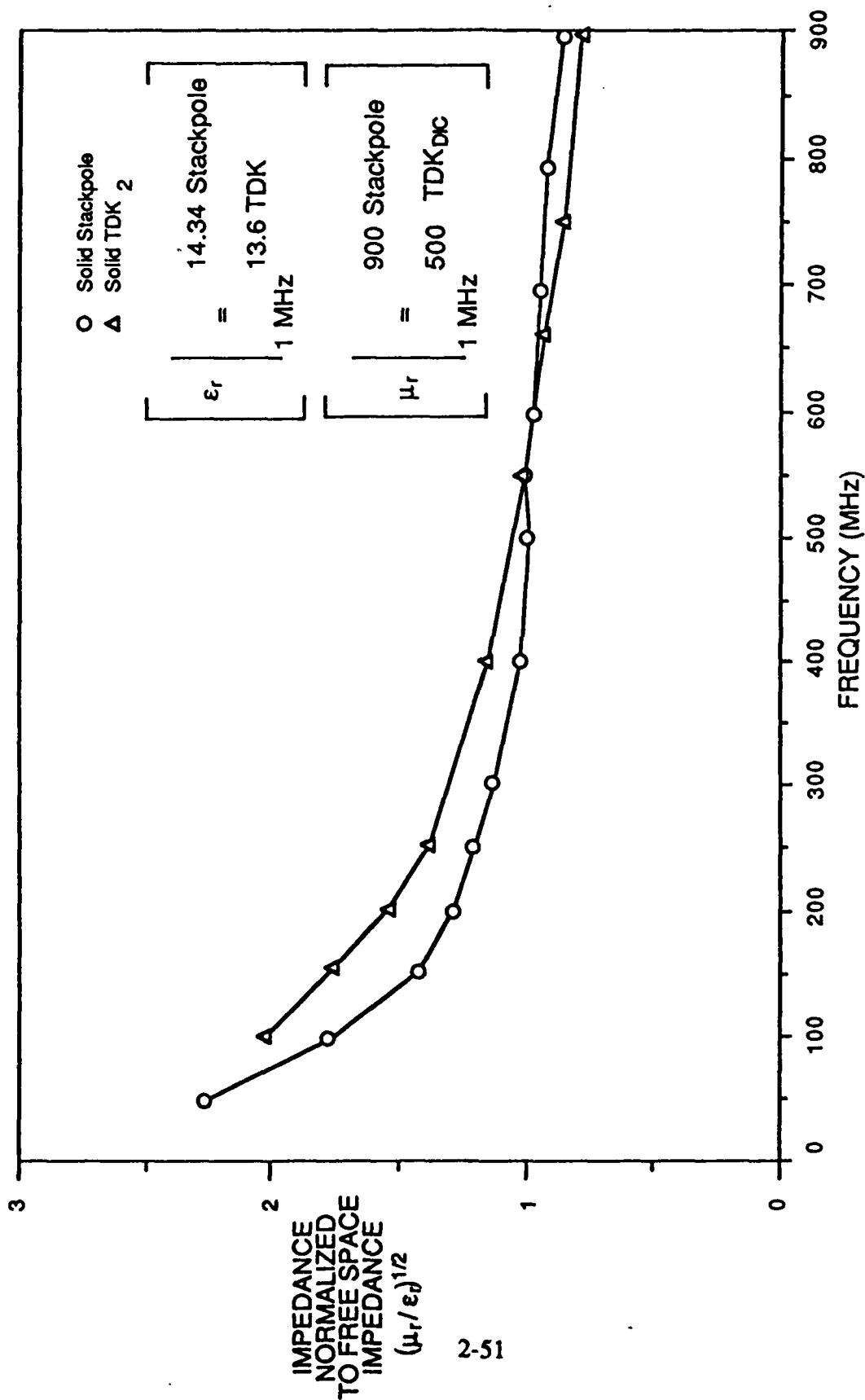


Figure 26: Impedance of ferrites normalized to free space impedance (377 Ω)

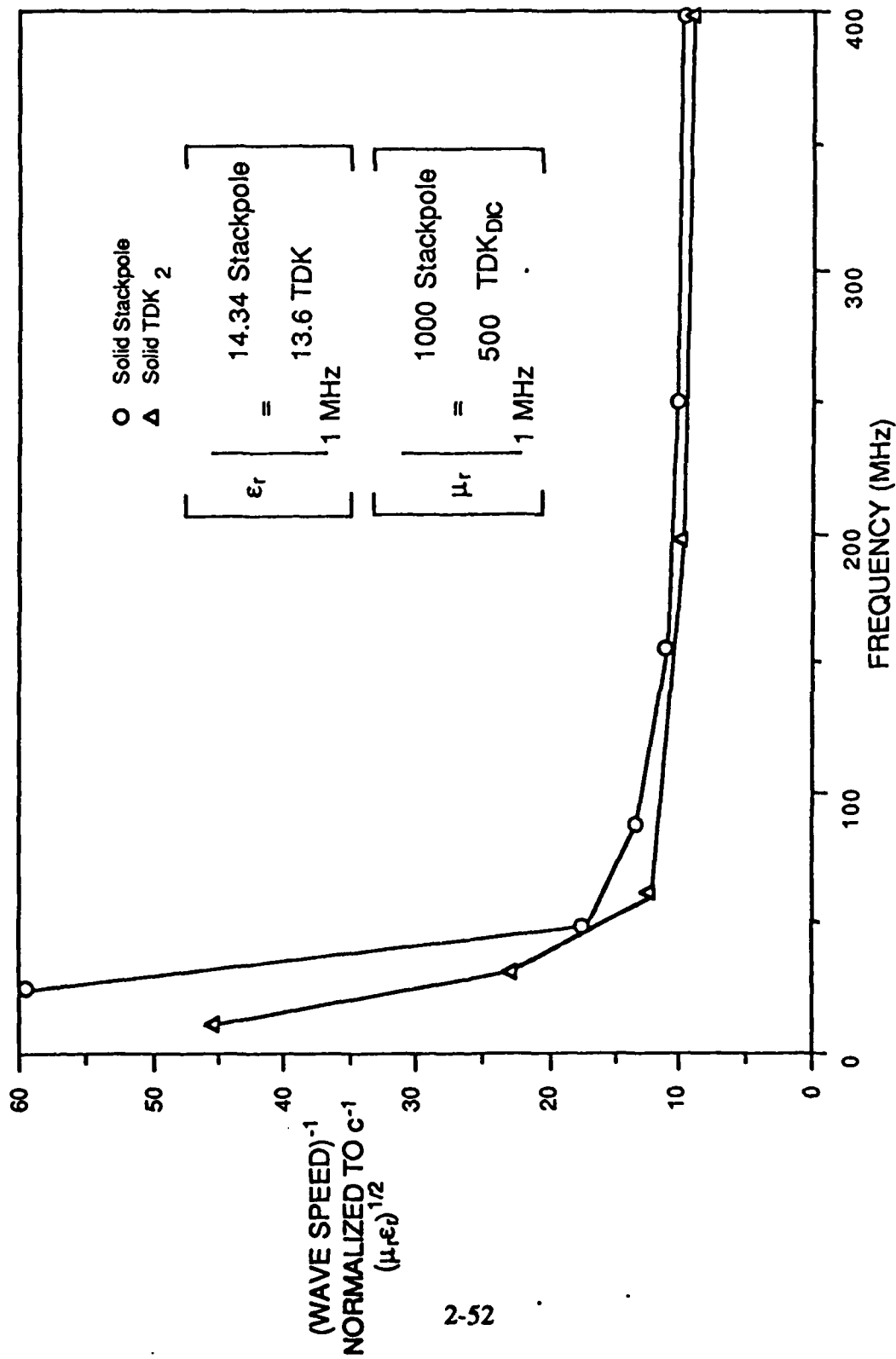


Figure 27: Inverse wave speed in ferrite normalized to c⁻¹

3.0 NEW INDUCTION ACCELERATOR ARCHITECTURES

In Section 3, we discussed the impact that the beam pipe diameter places on the required ferrite core volume and losses. The problem arises from the location in which the ferrite is placed in conventional induction accelerators. In conventional induction accelerators the ferrite is wrapped around the beam pipe and solenoid. Referring to Fig. 28 where we have stripped the induction accelerator schematic to its simplest essentials, we see that some provision must be made to isolate the shields of the coaxial drive cables which would otherwise attempt to float up to the potential of the previous induction cell. Since all of these cables connect to a common ground at the supply source, the accelerator would soon discover it was shorted out at the source. The time required for the accelerator to discover this is one roundtrip travel time along the drive cables. If the drive cables are long enough or the pulse short enough we would need no additional isolation.

In Fig. 29 we schematically depict the conventional method used to achieve one pulse length worth of isolation. As we discussed above, ferrite is wrapped around the beam pipe and the shields of the drive cables are connected to ground at the outer diameter of the ferrite. Placing the ferrite around the beam pipe uniquely determines the geometry, volume and efficiency of an induction cell as a function of only the pulse length, drive voltage per cell, and inherent ferrite properties. The length of each accelerator cell is set by the permeability and permittivity of the ferrite and the pulse length. The inner diameter of the ferrite is set by the beam pipe diameter and the radial extent of the ferrite core is determined by the drive voltage and available flux swing in the ferrite. Increasing the beam pipe diameter to reduce beam breakup growth results in increased ferrite volume and increased losses. In order to minimize losses, the ferrite inner diameter should be as small as possible but in order to improve beam stability the inner diameter should be as large as possible. This is the dilemma posed by the conventional linear induction accelerator design. We will however see that placing the ferrite around the beam pipe does have one key advantage. A ground shield can be used to tightly enclose the accelerator structure confining the electric field to the immediate vicinity of the accelerator gaps. No field

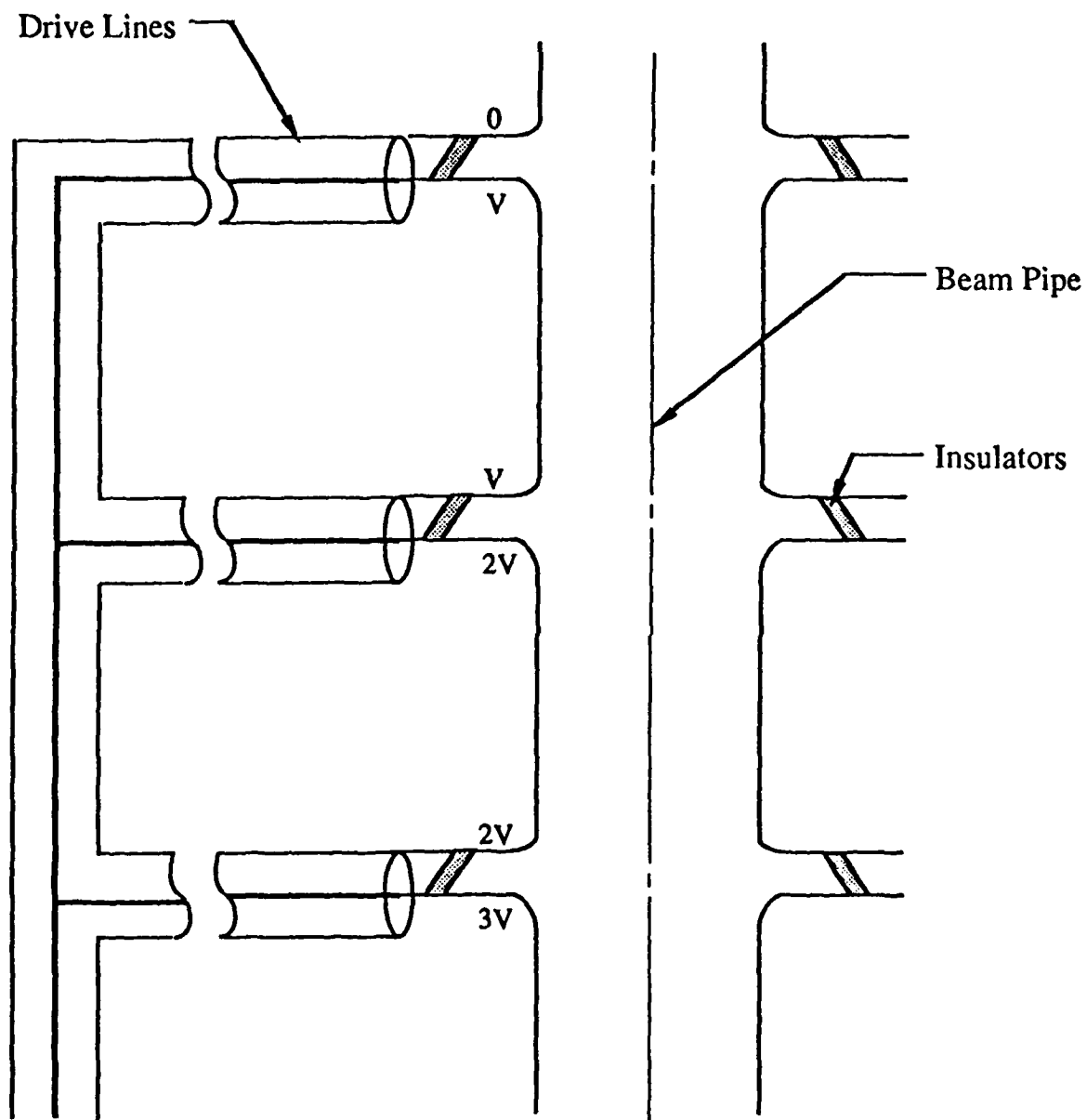
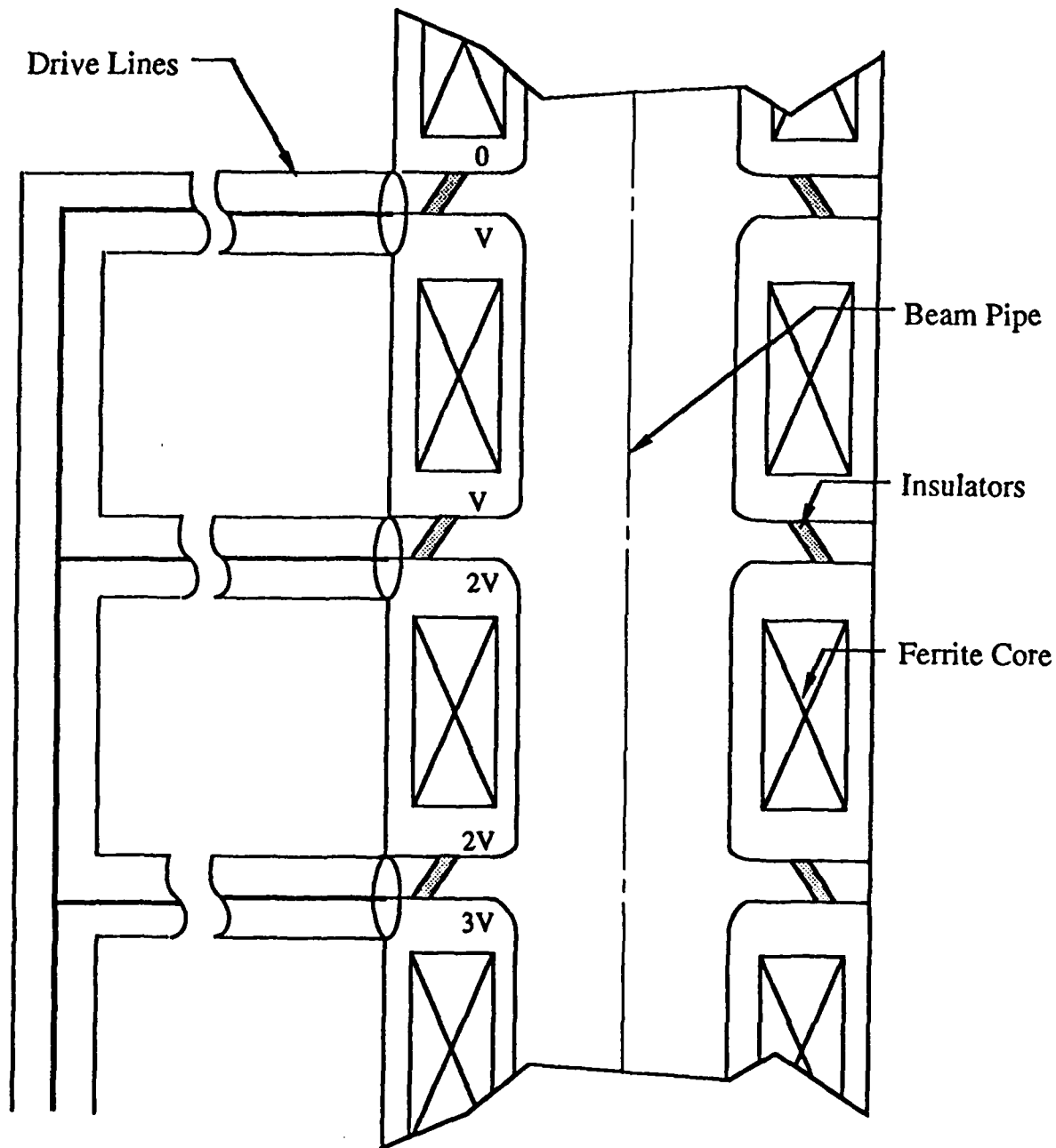


Figure 28: Simplified induction linear accelerator schematic



Core Length Set By Pulse Length
 Core ID Set By BBU (OD of Beam
 Pipe and Focussing Magnets)
 Core OD Set By Voltage per Cell

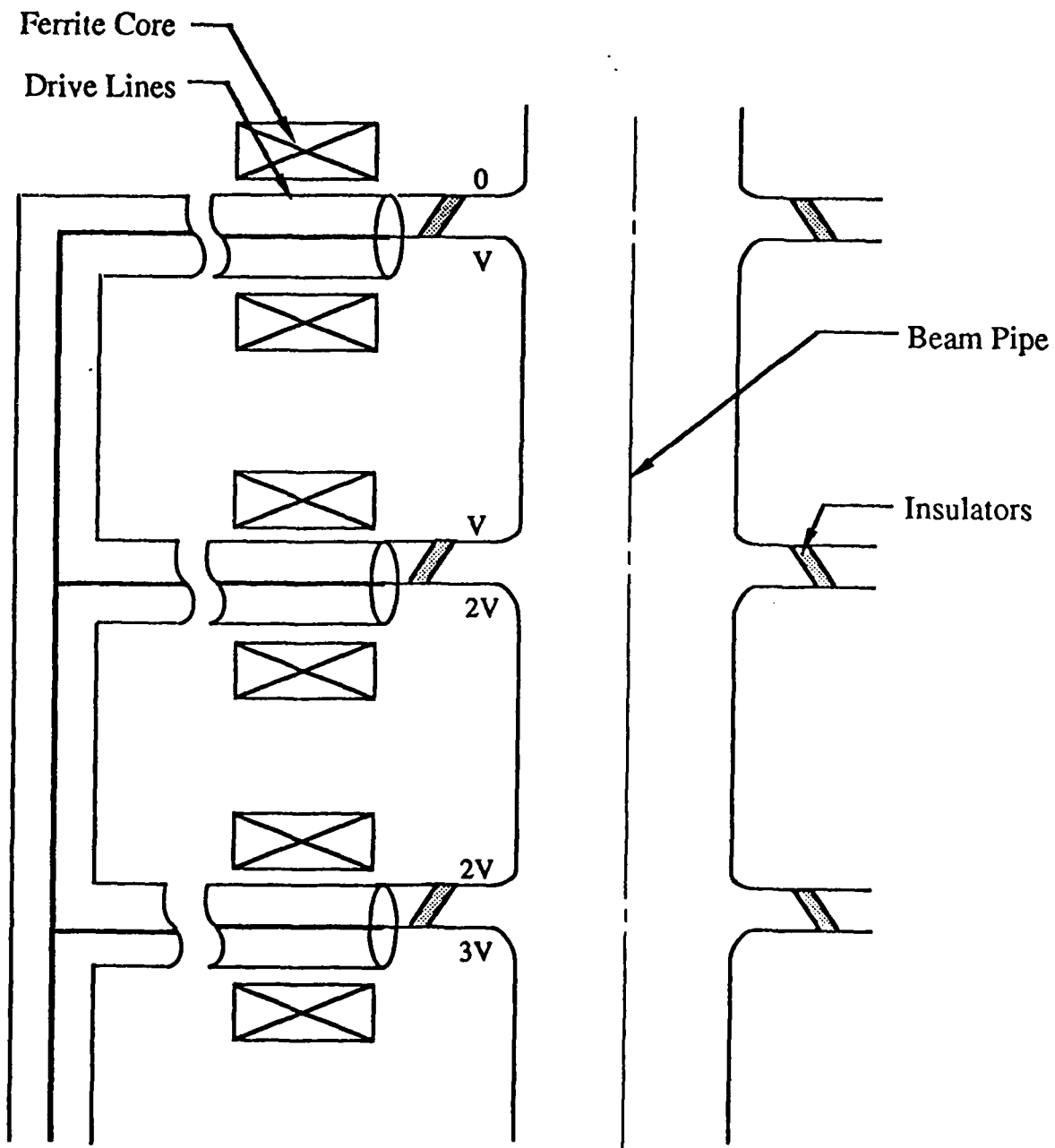
Figure 29: Conventional linear induction accelerator design

appears outside this ground shield and no voltages appear at any point which exceed the single cell voltage except inside the beam pipe.

In Fig. 30 we suggest a new induction linear accelerator configuration which leads to a more compact, lighterweight design. Here the beam pipe can be as large as desired as the ferrite is wrapped around the drive lines. As the drive lines are typically only 1-2 inches in diameter and the beam pipe plus focussing magnet are typically 10 inches or more in diameter, placing the ferrite around the drive lines reduces the ferrite volume requirement by two orders of magnitude. The gradient of the accelerator is no longer determined by the ferrite properties and for short pulses the inductance of a coiled drive line would be sufficient by itself to isolate the shields on the drive cables as depicted in Fig. 31. In fact the drivelines can be wrapped around ferrite cores several times. This can further decrease the ferrite volume required in the linear induction accelerator design (Concept I) shown in Fig. 30.

In the case of this modified induction accelerator design, the outer ground shield is optional. For space-based applications there is probably no reason to shield the accelerator and the accelerating field can simply be allowed to appear on the outside of the accelerator. An observer watching the unshielded accelerator would see an electromagnetic wave traveling down the length of the induction accelerator as the electron beam is accelerated. The length of this electromagnetic wave would simply be the pulse length multiplied by the speed of the accelerating electrons which would essentially be the speed of light. As an example, a 5 nanosecond accelerating pulse would appear as a wave approximately 5 feet in length. The peak amplitude of this wave is simply given by multiplying the gradient of the accelerator by the spatial pulse length and dividing by 2. For this reason we will see that it becomes very important to minimize the pulse length as this will determine the maximum voltage that appears on the outside of the accelerator at a given gradient.

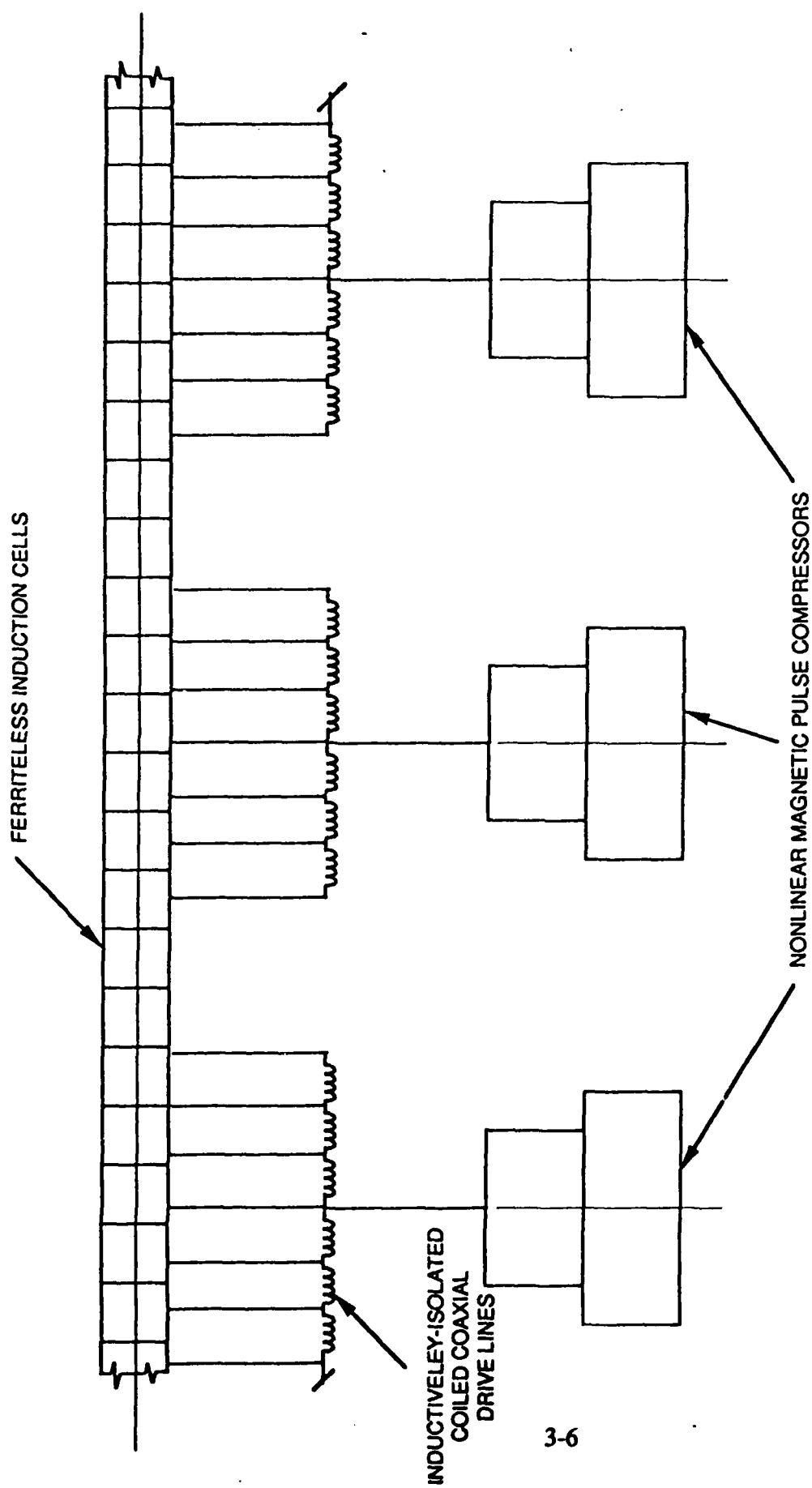
This external electromagnetic wave induces a voltage drop on the outer conductor of the drive lines which tie back to a common ground at either the pulsed power drive or optional external ground shield. The inductance associated with either the ferrite isolation cores or coiling the



Core ID Determined By Drive Line

$$\text{Core Cross-Section} = \frac{\text{Gradient} \cdot c \cdot (\text{pulse length})^2}{4}$$

Figure 30: Concept I - Modified linear induction accelerator



3-6

Figure 31: Concept II: Ferriteless induction accelerator for short pulse operation

transmission line must be sufficient to prevent significant current from flowing. The efficiency of the accelerating structure is reduced by the ratio of this leakage current to the accelerating electron beam current. The peak voltage drop across the isolation inductors is no longer the single cell voltage as in the case of the conventional linear induction accelerator but is given as

$$V_{peak} = \frac{\text{Gradient} \cdot \text{PulseLength} \cdot v_{electron}(\approx c)}{2}$$

As the wave travels past the isolation inductor, the voltage across the inductor drops to zero at the center of the wave and then reverses reaching a maximum negative voltage equal to the maximum positive voltage. The average voltage drop across the inductor is zero. This means that the ferrite cores are automatically reset. In the case of a conventional air core inductor, created by coiling the transmission line, all of the energy associated with the shunt leakage current is returned to the accelerating electrons.

As the electromagnetic wave travels down the accelerator at approximately the speed of light, the tail of the wave is feeding energy into the tail of the electron beam pulse and the head of the wave is being constantly recreated by the drive pulse to the next accelerator cell in line. Creating this wave front requires charging the stray capacitance between the next accelerator cell and the nearest ground plane to the peak voltage appearing across the isolation inductors.

The maximum one-way volt-second product determines the required ferrite core cross-section and/or the number of turns the drive lines makes around the core. From Faraday's law we derive.

$$\begin{aligned} N \cdot \text{Area} \cdot \Delta B_s &= \int V \cdot dt \\ &= V_{peak} \frac{\text{PulseLength}}{4} = \frac{\text{Gradient} \cdot (\text{PulseLength})^2 \cdot c}{8} \end{aligned}$$

The maximum voltage to ground is identical to the peak voltage across the isolation core, but it is a dipole field and falls off very rapidly with distance in the radial direction.

As an example we will examine the properties of a conceptual accelerator whose specifications appear in Table II. In this lightweight accelerator the gradient is 3 MeV/meter and the pulse length is 5 nanoseconds. If the electron beam is travelling at approximately the speed of

Table II: Compact, Lightweight Induction Linear Accelerator Specifications

Acceleration Potential	- 150 MeV
Beam Current	- 2600 Amperes
Pulse Length	- 5 nsecs
PRF	- 50 kHz
Average Beam Power	- 100 MW
Gradient	- 3 MeV/meter
Beam Energy/Pulse	- 2000 Joules
Overall Accelerator Mass	- 10,000 kg

light, then the peak voltage across the isolation inductors is 2.25 MeV. The volt-second product appearing across the isolation inductor is only 2.81 volt-milliseconds. The single turn ferrite core cross-section requirement, assuming a ΔB_c of 6000 Gauss, is only 7 square inches. If we assume a drive line diameter of 1 inch operating at 150 kV then a single turn ferrite core with dimensions of 1" ID X 2" OD X 14" long is all that is required. Such a core would weigh approximately 2 kg. If each drive line is supplying 150 kV to the accelerator then there would be 1000 accelerator cells in our 150 MeV accelerator and the total ferrite core weight would be only 2000 kg. We will see that by invoking another design option, it will be possible to reduce the required ferrite volume by a factor of 4 and the weight down to 500 kg. The focusing magnets are wrapped around the beam pipe and power is supplied by wires fed up through the center of the drive line inner conductor.

As an interesting comparison, a 150 MeV induction accelerator of conventional design operating with a 50 nanosecond accelerating pulse and a 1 foot diameter beam pipe would have required over 200,000 kg of ferrite. In the case of the conventional induction accelerator this weight would increase linearly with the pulse length. In the Concept I induction accelerator design, the weight increases with the square of the pulse length. If the pulse length were decreased even more, the weight savings would be even greater. Conversely if the pulse length is increased, the weight savings are not as great. The development of short pulse driver technology is paramount to increasing the utility and decreasing the cost and weight of all induction accelerators, but it is an especially critical issue in the case of these alternate design concepts. For very long pulses of order several hundred nanoseconds, the conventional induction accelerator design will always be the preferred approach, but any induction accelerator operating for these pulse lengths is prohibitively large and of very limited utility.

As we mentioned above the drive pulse to each accelerator cell must charge up the stray capacitance between the cell and the nearest ground plane to the peak voltage across the isolation inductor. In our 5 nanosecond pulse length, 3 MeV/meter accelerator we found the peak voltage to ground was 2.25 MeV. If we assume a 150 kV/cell drive voltage then each accelerator cell

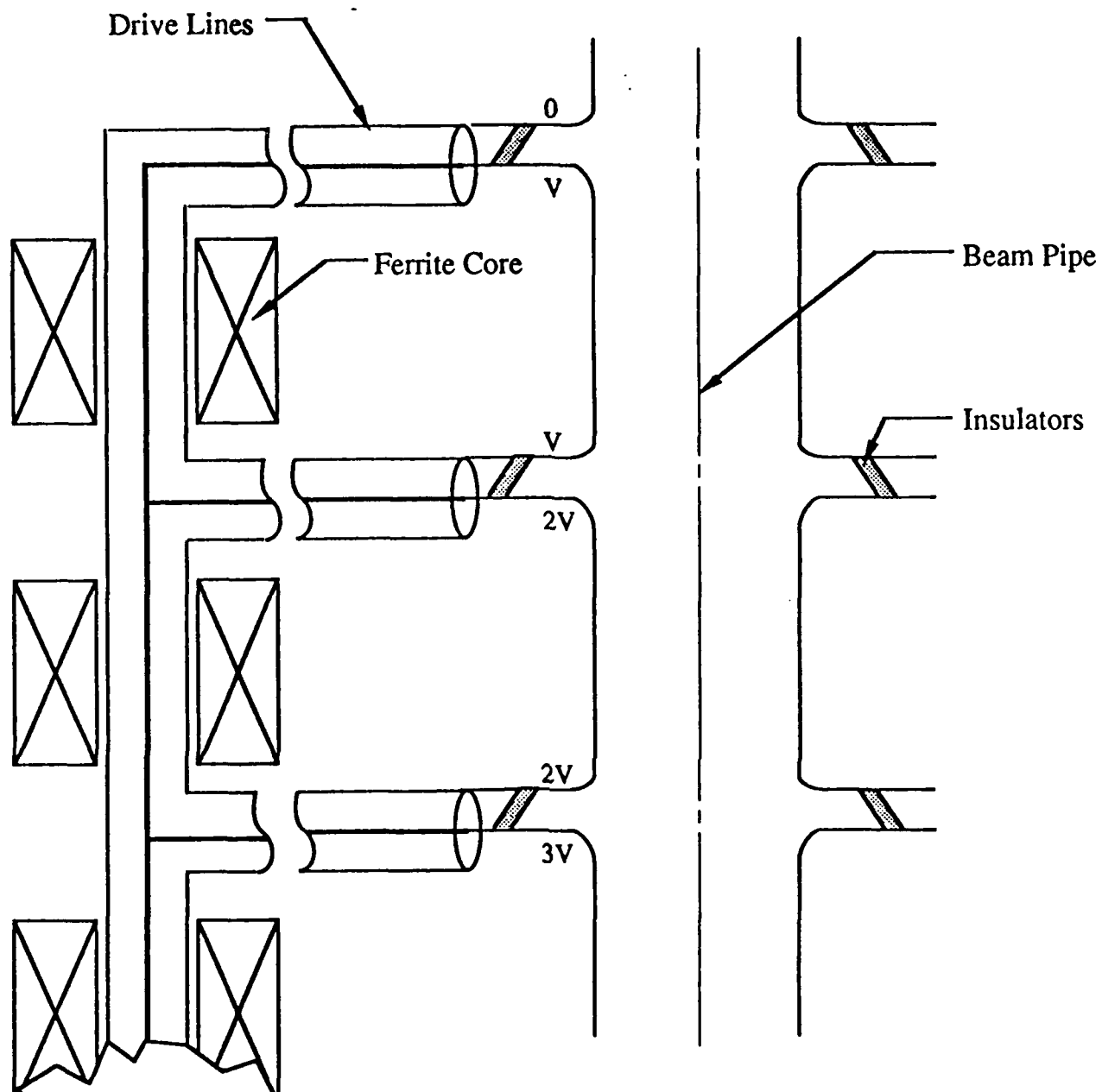
is 5 centimeters in length. If we were to place our 1 foot diameter beam pipe inside of a 6 foot diameter thin walled metal tube or aluminized balloon for shielding purposes, then the capacitance per unit length is given as

$$C = \frac{2\pi\epsilon_0}{\ln(R_o/R_i)} = 30pf/meter$$

For our 5 centimeter long accelerator cell, the incremental capacitance to ground is 1.5 picofarads. Charging this capacitance to 2.25 MeV would require approximately 3.4 microcoulombs. Referring to Table II we see that we are planning to accelerate an electron beam current of 2600 amperes. At this drive level, it would require 1.25 nanoseconds to charge the stray capacitance. This should pose very little problem as the energy corresponding to this 1.25 nanoseconds of electron beam pulse will be fed into the beam at the tail of the pulse. The accelerating pulse must simply arrive at the accelerating cells 1.25 nanoseconds ahead of the electron beam pulse for optimum coupling efficiency. Both the drive pulse and the electron beam pulse would still be 5 nanoseconds in duration.

Finally in Fig. 32 we present a third design option known as Concept III. The Concept III induction accelerator design can be combined with the Concept I accelerator design. By grouping the accelerator cells in blocks fed by a common drive line we can further reduce the ferrite requirement. For instance if we were to block accelerator cells together in groups of 10 in our example, then only one primary stem drive line would have to be isolated from ground for each group of 10 accelerator cells. The isolation inductors placed between the individual cells need only be sufficient to provide 150 kV isolation for the 5 nanosecond drive pulse. As these cores are wrapped around the 1 inch drive line rather than the 1 foot diameter beam pipe the ferrite volume requirement is reduced by more than two orders of magnitude for these 150 kV isolation inductors over the conventional induction linear accelerator design. Employing this design in our example accelerator would reduce the ferrite weight to less than 500 kg.

In summary we have described some alternate induction linear accelerator designs which offer significant weight and cost savings over conventional induction accelerator designs while decreasing the length of the accelerator by a factor of 6. These alternate designs are not the



Core Volume Reduced By $\frac{(\text{Drive Line Diam.})^2}{(\text{Beam Pipe} + \text{Magnet Diam.})^2} \sim 100$
Over Conventional Induction Accelerator

Figure 32: Concept III - Modified induction accelerator

optimum choice for all applications but offer many advantages in short pulse and/or space based applications.

3.1 Summary of Phase I Effort

Under the Phase I effort, SRL has undertaken a detailed investigation into the properties of ferrite as they apply to the design of induction linear accelerators. This research has included both analytical studies and experimental measurements. Ferrite properties have been documented over a wide range of compositions and operating pulse lengths.

In addition to these ferrite studies, SRL has undertaken an investigation into the basic foundations of induction accelerator design. These studies were aimed at developing new design techniques and architectures which might lead to size, cost, and weight reductions along with increased accelerating gradients. SRL has identified and documented the limiting features in conventional induction linear accelerator designs and has developed several new architectures which may circumvent these limitations.

In the Phase I effort, the design of induction linear accelerators was studied. The function of the ferrite in the accelerator cells was thoroughly analyzed and the key parameters were determined. Test fixtures were assembled so as to be able to evaluate the performance of different ferrite compositions in these areas. Samples of ferrite were purchased which spanned the entire range of useful compositions. The performance of these compositions was evaluated over the range of applicable operating frequencies. The experimental data was fully documented and presented in a manner which allowed for a simple evaluation of the optimum compositions for various pulse lengths and applications.

Also included in the Phase I study was the investigation of alternative induction cell architectures which might be better optimized for use in FEL applications. Several improved designs were developed which led to new compact, lightweight, low cost induction linear accelerator architectures.